

# The Effects of Wind Farm Wakes on Freezing Sea Spray in the Mid-Atlantic Offshore Wind Energy Areas

David Rosencrans<sup>1,2</sup>, Julie K. Lundquist<sup>1,2,3</sup>, Mike Optis<sup>2,4</sup>, and Nicola Bodini<sup>2</sup>

<sup>1</sup>Department of Atmospheric and Oceanic Sciences, University of Colorado, Boulder, 80303, USA

<sup>2</sup>National Renewable Energy Laboratory, Golden, 80401, USA

<sup>3</sup>Renewable and Sustainable Energy Institute, Boulder, 80303, USA

<sup>4</sup>Veer Renewables, Courtenay, V9N 9B4, Canada

Correspondence to: David Rosencrans (David.Rosencrans@Colorado.edu)

## Abstract

The U.S. is expanding its wind energy fleet offshore where winds tend to be strong and consistent. In the mid-Atlantic, strong winds, which promote convective heat transfer and wind-generated sea spray, paired with cold temperatures can cause ice on equipment when plentiful moisture is available. Near-surface icing is induced by a moisture flux from sea spray, which poses a risk to vessels and crews. Ice accretion on turbine rotors and blades occurs from precipitation and in-cloud icing at temperatures below freezing. Ice accretion induces load and fatigue on mechanical parts which reduces blade performance and power production. Thus, it is crucial to understand the icing hazard across the mid-Atlantic. We analyze Weather Research and Forecasting model numerical weather prediction simulations at coarse temporal resolution over a 21-year period to assess freezing [sea spray](#) events over the long-term record and at finer granularity over the 2019–2020 winter season to identify the post-construction turbine impacts. Over the 2019–2020 winter season, results suggest that sea-spray–induced icing can occur up to 67 hours per month at 10 m at higher latitudes. Icing events during this season typically occur during cold air outbreaks (CAO), which are the introduction of cold continental air over the warmer maritime surface. During the 2019-2020 winter season, CAO lasted a total duration of 202 hours. While not all [freezing sea spray](#) events occurred during CAO over the 21 year period, all CAO events had FSS present. Further, we assess the turbine–atmosphere impacts of wind plant installation on icing using the fine-scale simulation data set. Wakes from large wind plants reduce the wind speed which mitigates the initiation of sea spray off white-capped waves. Conversely, the near-surface turbine-induced introduction of cold air in frequent wintertime unstable conditions enhances the risk for freezing. Overall, the turbine–atmosphere interaction causes a small reduction of FSS hours within the wind plant areas, with a reduction up to 15 hours in January at the 10 and 20 m heights.

## 1 Introduction

The offshore wind energy industry is undergoing rapid growth to supply emissions-free energy to the electrical grid. In the U.S., offshore capacity targets are approaching 40 GW by 2040 (Musial et al., 2022). Capacity expansion into relatively cold offshore regions will subject turbines to harsher wintertime conditions, which necessitate an understanding of the hazards that marine icing poses to offshore wind turbines, service vessels, and crew safety.

Formatted: Font color: Text 1

Deleted: FSS

Formatted: Font color: Text 1

39

40 Ice accretion reduces the aerodynamic efficiency of the turbine blade, which hinders energy capture and annual  
41 energy production (Battisti et al., 2006; Kraj and Bibeau, 2010; Wei et al., 2020). Ice can remain on the rotors even  
42 after freezing conditions end, as slow natural processes such as ice shedding and melting extend the limitation to  
43 energy yield (Gao and Hong, 2021). One study found that excessive icing induced a power loss of 63 % for a single  
44 turbine over a 51-h icing event (Gao and Hu, 2021). Faster winds during cold front passages can enhance wind-  
45 energy supply during high-load cold-weather events, although, following frontal passages, the combination of cold  
46 temperatures and slow wind speeds may pose severe challenges for utility grid planners (Novacheck et al., 2021).  
47 Despite the energy losses from ice accretion, various strategies can mitigate or even prevent ice accretion altogether  
48 (IEA, 2018; Madi et al., 2019). While turbine blade icing is well studied (IEA, 2018; Martini et al., 2021; Contreras  
49 Montoya et al., 2022), icing near the turbine base, affecting operations and maintenance activities, is not.

50

51 The leading causes for low-level offshore icing are wave-impact and wind-induced sea spray (Dehghani-Sanij et  
52 al., 2017). Sea spray provides nuclei for ice clouds at high latitudes where airborne dust is sparse, being lofted by  
53 bursting bubbles and droplets from white-capped waves (Russell, 2015; Dehghani-Sanij et al., 2017). Ice  
54 accumulation from spray raises the center of gravity of ships, which can cause loss of stability and lead to capsizing  
55 (Guest and Luke, 2005). Observations suggest that the liquid droplets torn off of white caps, referred to as spume,  
56 experience a marked increase in concentration with strong winds above  $9 \text{ m s}^{-1}$  (Ross and Cardone, 1974; Monahan  
57 et al., 1983; Monahan and MacNiocaill, 1986). Further, spray particles more easily supercool with cold sea surface  
58 temperatures (SST) below  $7^\circ \text{ C}$  and at air temperatures below the freezing point for saline ocean water at  $-1.7^\circ \text{ C}$   
59 (U.S. Navy, 1988; Guest and Luke, 2005). Ice accumulation is believed to have caused the recent losses of three  
60 ships, including 1) the *Destination*, which sank near St. George Island, Alaska in 2017 (Kraegel, 2018); 2) the  
61 *Scandies Rose*, which sank southeast of Kodiak, Alaska, in 2019 (NTSB, 2021); and 3) the *Omega*, which sank in the  
62 Barents Sea in 2020 (Nilsen, 2020). To mitigate ice-induced accidents, inclement weather forecasts are furnished for  
63 coastal waters. A Coastal Waters Forecast, delivered by the National Weather Service, will contain a “freezing spray  
64 advisory” if freezing water droplets can accumulate on vessels due to a combination of SST, wind speed, air  
65 temperature, and vessel motion (Glossary - NOAA’s National Weather Service, 2023). At accumulation rates greater  
66 than  $2 \text{ cm h}^{-1}$ , the advisory becomes a “heavy freezing spray watch”.

67

68 Wind turbines can modify the amount and severity of icing conditions via competing effects. Enhanced  
69 turbulence caused by spinning blades transports heat from aloft to lower altitudes within the rotor-swept region or  
70 near the surface. In stable stratification, warmer potential temperatures are transported downward, which introduces  
71 a near-surface warming effect, and vice versa in unstable conditions (Fitch et al., 2013; Rajewski et al., 2013; Xia et  
72 al., 2016; Siedersleben et al., 2018; Tomaszewski and Lundquist, 2020). However, recent research suggests taller  
73 turbines may reverse this phenomenon (Golbazi et al., 2022) depending on the depth of the atmospheric boundary  
74 layer (Quint et al., 2024). As the winter months feature more frequent unstable stratification along the U.S. East  
75 Coast (Bodini et al., 2019), turbine-induced cooling may increase the potential for near-surface freezing. In contrast,

76 turbines harness momentum from the flow, which reduces the downwind wind speed (Nygaard, 2014; Platis et al.,  
77 2018; Schneemann et al., 2020). A reduction in wind speed conversely reduces the potential for icing (Dehghani-  
78 Sanij et al., 2017). Thus, it is crucial to understand how large-scale wind deployment across the mid-Atlantic will  
79 modify the regularity and intensity of freezing sea spray (FSS) conditions.

80

81 Herein, we employ numerical weather prediction modeling to quantify the baseline offshore icing risk and the  
82 wind plant post-construction effects. Section 2 outlines the modeling setup and discusses the techniques for  
83 discerning icing conditions and cold air outbreak events. Section 3 reports results for the spatiotemporal icing risk,  
84 causal factors, and the adjustments by wind plants. Section 4 offers concluding remarks and discussion.

85

## 86 **2 Methods**

### 87 **2.1 NOW-23**

88 We explore annual variability of FSS conditions using the 2023 National Offshore Wind (NOW-23) data set  
89 (NREL, 2020; Bodini et al., 2024). This data set quantifies wind resources spanning all offshore regions of the  
90 United States for more than 20 years using the Weather Research and Forecasting (WRF) model version 4.2.1  
91 (Powers et al., 2017). We acquire model output at an hourly temporal resolution for the 21-year period from 01  
92 January 2000 to 31 December 2020. A parent domain feeds into an inner nested domain with horizontal grid  
93 resolutions of 6 km and 2 km, respectively. Both domains incorporate a vertical grid resolution of 5 m near the  
94 surface with stretching to 45 m aloft, using 61 vertical levels up to a 50 hPa top. The European Centre for Medium  
95 Range Weather Forecasts 5 Reanalysis (ERA5) dataset supplies hourly initial and boundary conditions at a 30 km  
96 resolution to WRF (Hersbach et al., 2020). NOW-23 employs the MYNN2 planetary boundary layer and surface  
97 layer (Nakanishi and Niino, 2006) schemes, eta microphysics (Ferrier et al., 2002), the Noah Land Surface Model  
98 (Tewari et al., 2004), the rapid radiative transfer model for shortwave and longwave radiation (Iacono et al., 2008),  
99 and the Kain–Fritsch cumulus parameterization (Kain, 2004) in the outmost domain only. For the mid-Atlantic  
100 region, NOW-23 was validated against observations from three ZephIR ZX300M floating lidars (Pronk et al., 2022).

101

### 102 **2.2 NOW-WAKES**

103 We explore the seasonal variability and impacts of wind plants on icing conditions using high-fidelity numerical  
104 weather prediction simulations over the period 01 September 2019 to 31 August 2020. These validated WRF version  
105 4.2.1 simulations are described in detail in Rosencrans et al., (2024) but are summarized here for the reader's  
106 convenience. This period is chosen for the availability of lidar measurements for validation of the wind speed  
107 profile. A parent domain hosts an inner nest with horizontal grid resolutions of 6 km and 2 km, respectively (Figure  
108 1). Both domains include a vertical grid resolution of 10 m near the surface with stretching aloft, using 54 vertical  
109 levels up to a 50 hPa top. The inner domain outputs data at an instantaneous history file frequency of 10 minutes.  
110 Constant time steps are set to 18 s and 6 s in the outer and inner domains, respectively. Initial and boundary  
111 conditions are also supplied by the hourly 30 km ERA5 dataset (Hersbach et al., 2020). Lower boundary conditions  
112 are provided as SST by the UK Met Office Operational Sea Surface Temperature and Sea Ice Analysis dataset  
113 (Donlon et al., 2012) and show good agreement during validation against mid-Atlantic bight buoys (Redfern et al.,

2023). Physics parameterizations include the MYNN2 planetary boundary layer and surface layer (Nakanishi and Niino, 2006), the Noah Land Surface Model (Niu et al., 2011), the New Thompson microphysics (Thompson et al., 2008), the rapid radiative transfer model for longwave and shortwave radiative transfer (Iacono et al., 2008), and the Kain–Fritsch Cumulus (Kain, 2004) schemes. The Kain–Fritsch cumulus parameterization applies to the parent domain only. We incorporate spectral nudging to relax model output toward the ERA5 boundary conditions in the inner domain. We apply a cutoff wavenumber of 3 (Gómez and Míguez-Macho, 2017), above which model dynamics may resolve freely. No nudging is applied beneath the boundary layer height.

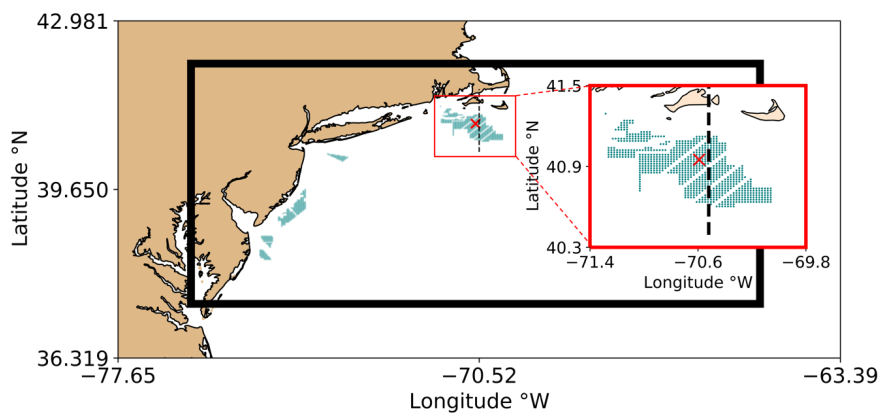


**Figure 1. Modeling domains. The entirety of the outer domain with inner domain is shown, outlined by the black rectangle. The red square is zoomed in on the Rhode Island–Massachusetts (RIMA) block to enhance visibility. Turbines are shown as teal dots. The red “X” indicates the point of interest (POI) where time series are acquired. The dashed black line is a cross section extending through the RIMA block.**

We incorporate the effects of wind turbines using the WRF wind farm parameterization (WFP) (Fitch et al., 2012). WFP simulations feature wind plant layouts of the lease areas and include 1,418 turbines (Figure 1, Table 1). The WFP incorporates the effects of turbines by implementing a drag-induced deceleration of wind flow and an addition of turbulence at model levels intersecting the rotor area. We execute WFP simulations adding both 0 % and 100 % turbulent kinetic energy (TKE) (Rosencrans et al., 2024), although a smaller value of 25 % in some cases agrees better with neutrally stratified large-eddy simulations (Archer et al., 2020). Differences in the number of icing hours between 0 % and 100 % added TKE are slight, so we report those from 100 % added TKE only. Thus, for the remainder of this article we refer to the 100 % added TKE simulation as “WFP”. This work utilizes 12 MW GE Haliade wind turbines with a 138 m hub height and 215 m rotor diameter, which are scaled by Beiter et al. (2020) from a 15 MW reference turbine. We carry out separate simulations using both no wind farms (NWF) and wind farms (WFP) for the full year-long period from 01 September 2019 to 31 August 2020 (Table 1).

Deleted: Figure 1

Deleted: Table 1

Formatted: Check spelling and grammar

Formatted: Check spelling and grammar

Deleted: Table 1

Formatted: Check spelling and grammar

143 **Table 1. List of NOW-WAKES WRF simulations characterized by turbine characteristics. The simulation period**  
 144 **spans 01 September 2019 to 01 September 2020.**

Simulation type	Acronym	Turbine rated power	Added TKE	# Turbines
No Wind Farms	NWF	N/A	N/A	0
Wind Farm Parameterization	WFP	12 MW	100 %	1,418

145  
 146 **2.3 Icing hours detection**  
 147 Ice accretion occurs when supercooled water freezes upon contact with objects. The largest contributions to sea  
 148 spray icing are provided by the bursting of bubbles and advection of spray from white-capped waves (Dehghani-  
 149 Sanij et al., 2017). In the presence of moisture, three key variables dictate offshore freezing conditions: wind speed,  
 150 SST, and air temperature (Overland et al., 1986; Overland, 1990; Guest and Luke, 2005; Dehghani-Sanij et al.,  
 151 2017; Line et al., 2022).

152  
 153 We detect FSS conditions following common thresholds defined by the latter studies (Guest and Luke, 2005;  
 154 Dehghani-Sanij et al., 2017; Line et al., 2022). These criteria require 1) wind speeds in excess of  $9 \text{ m s}^{-1}$ , 2) air  
 155 temperatures below  $-1.7^\circ \text{ C}$ , and 3) SST less than  $7^\circ \text{ C}$ . Air temperature and SST thresholds can range between  $-2^\circ$   
 156  $\text{C}$  and  $-1.7^\circ \text{ C}$  and between  $5^\circ \text{ C}$  to  $8.9^\circ \text{ C}$ , respectively, as reviewed by Dehghani-Sanij et al., (2017). As such, we  
 157 provide a sensitivity assessment for the full range (Appendix B). The surface skin temperature (WRF output variable  
 158 “TSK”) is assessed because the SST field inherits coarse blocks of missing data around coastlines from the ERA5  
 159 dataset. The resulting spatial maps are masked by the land use (WRF output variable “LU\_INDEX”) to ensure that  
 160 icing conditions over land are not counted. The number of 10 min timestamps where these criteria are met each  
 161 month are recorded for all simulations. As sea spray often lofts to between 5 and 20 m above sea level (Dehghani-  
 162 Sanij et al., 2017), we quantify sea spray-induced icing at the 10 and at 20 m heights. For the 20 m conditions, we  
 163 use 20 m air temperatures but use 10 m wind speeds as those winds have been linked to the generation of spray off  
 164 white-capped waves (Dehghani-Sanij et al., 2017; Guest and Luke, 2005; Line et al., 2022; Ross and Cardone, 1974;  
 165 Monahan et al., 1983; Monahan and MacNiocaill, 1986).

166  
 167 Due to the height constraint of sea spray particles, we consider both precipitation-based and in-cloud icing at the  
 168 138 m hub height by assessing different criteria for 1) the nonzero presence of liquid rain water (WRF variable  
 169 “QRain”) that may become supercooled at temperatures less than  $0^\circ \text{ C}$ , 2) ice (WRF variable “QICE”), and 3) the  
 170 aggregation from snow (WRF variable “QSNOW”) (Parent and Ilinca, 2011; ISO, 2017). Further, we detect cloud or  
 171 fog formation when 4) the relative humidity (RH) is greater than or equal to 100% following:

$$e_s = e_0 \exp \left[ \frac{b(T - T_1)}{(T - T_2)} \right] \quad (1)$$

$$w_s = \frac{\epsilon e_s}{p - e_s} \quad (2)$$

174 
$$RH = \frac{w}{w_s} \times 100\% \quad (3)$$

175 where  $e_s$  is the saturation mixing ratio,  $e_0$  is 6.112 mb,  $b$  is 17.67,  $T_1$  is 273.15 K,  $T_2$  is 29.65 K,  $T$  is the air  
 176 temperature,  $\epsilon$  is 0.622,  $p$  is the atmospheric pressure, and  $w$  is the mixing ratio (WRF output “QVAPOR”) (Stull  
 177 B., 1988). None of the aforementioned criteria must occur at the same time for icing to occur. However, we require  
 178 that one must occur in conjunction with an air temperature less than 0° C for an icing event.

179

180 **2.4 Ice accumulation rate**

181 A predictability function assesses the likelihood for freezing in the presence of sea spray. We assess the  
 182 predictability of icing conditions at the point of interest (POI) in the Rhode Island/Massachusetts (RIMA) block  
 183 (Figure 1) separately from the NOW-WAKES and the NOW-23 datasets. The predictability ( $PR$ ) for sea spray–  
 184 induced ice formation follows:

185 
$$PR = \frac{V_a(T_f - T_a)}{1 + 0.4(T_s - T_f)} \quad (4)$$

186 where  $V_a$  is the wind speed,  $T_f$  is the temperature threshold of  $-1.7^\circ$  C,  $T_a$  is the air temperature, and  $T_s$  is the SST  
 187 (Guest and Luke, 2005; Overland et al., 1986; Overland, 1990). A humidity variable is not present in Eq. (4) due to  
 188 the assumption that sea spray introduces a constant source of moisture during fast winds. A group of successive  
 189 timestamps with nonzero PR are considered the same event. Separate flagged timestamps occurring within 24 hours  
 190 of each other span the same synoptic regime (Winters et al., 2019), and so the entire duration between the two  
 191 flagged timestamps is considered one event. We additionally tested a threshold of 72 hours to account for synoptic  
 192 conditions spanning a longer duration but found that one FSS event lasted for over a week and our three FSS criteria  
 193 were only met 8 % of the time during the event. As such, the 72-h threshold was not justified.

194

195 **Table 2. Icing rate by PR. Rows delineate the PR value, icing class, and ice accretion rate. Columns delineate the icing**  
 196 **rate per PR range. From Guest and Luke (2005).**

PR	<0	0–22.4	22.4–53.3	53.3–83.0	>83.0
Icing Class	None	Light	Moderate	Heavy	Extreme
Icing Rate [cm h <sup>-1</sup> ]	0	<0.7	0.7–2.0	2.0–4.0	>4.0

197

198 The magnitude of PR can determine the rate of ice accretion (Table 2). The ice accretion rates are a general  
 199 guideline developed for 20 to 75 m long vessels; specific rates depend on the type of ship, its load, heading relative  
 200 to the prevailing wind direction, and its handling characteristics (U.S. Navy, 1988; Guest and Luke, 2005). For  
 201 instance, a larger ship requires faster winds and taller waves for sea-spray–induced ice to accumulate on a higher  
 202 deck but is more vulnerable to the prevailing wind direction due to reduced maneuverability. It is not known how  
 203 these icing rates would apply to wind turbines or to the vehicles used to access offshore wind turbines.

204

205 **2.5 Cold air outbreak detection**

206 Freezing conditions can be stimulated by the advection of cold continental air over a warmer maritime surface.  
207 The resulting temperature profile causes thermal instability, which can induce filamentary convective rolls that align  
208 to make cloud “streets” with parallel columns of ascending and descending air that transform into open convective  
209 cells further offshore (Geerts et al., 2022). Convective rolls can be used to identify cold air outbreak (CAO)  
210 (Atkinson and Wu Zhang, 1996; Geerts et al., 2022) and may also contribute moisture for in-cloud icing if the lifting  
211 condensation level is at or below rotor-swept heights. A quantitative approach proposed by Vavrus et al. (2006)  
212 identifies a cold air outbreak (CAO) by the magnitude and duration of anomalous air temperature, which we apply at  
213 the POI (Figure 1). This strategy requires that the near-surface temperature be at least 2 standard deviations below  
214 the wintertime average following Eq. (5):

215 
$$T < \bar{T} - 2(\sigma) \quad (5)$$

216 where  $T$  is the 2 m temperature,  $\bar{T}$  is the average 10 m temperature over the entire wintertime period, and  $\sigma$  is the  
217 standard deviation. The wintertime period spans November through March at a 10 min frequency to account for all  
218 non-zero-freezing predictability events. Again, successive timestamps with detected CAO are considered a single  
219 event, and separate events occurring within a 24 h span are conglomerated into the same event.

220  
221 **2.6 Atmospheric stability**

222 Turbulence from wind turbines modifies the near-surface temperature based on the atmospheric stability or  
223 stratification. We calculate the modeled atmospheric stability using the Obukhov Length ( $L$ ) (Monin and Obukhov,  
224 1954) (Eq. 6), which delineates the height above the surface at which buoyant turbulence equals mechanical shear  
225 production of turbulence, at a point centered on the RIMA block of lease areas:

226 
$$L = -\frac{u_*^3 \bar{\theta}_v}{\kappa g (\overline{w' \theta_v'})} \quad (6)$$

227 where  $u_*$  (UST in WRF output) is the friction velocity,  $\bar{\theta}_v$  is the virtual potential temperature,  $\kappa$  is the von Kármán  
228 constant of 0.4,  $g$  is gravitational acceleration of  $9.81 \text{ m s}^{-2}$ , and  $\overline{w' \theta_v'}$  (HFX in WRF output) is the surface dynamic  
229 heat flux converted into kinematic heat flux. Negative lengths between 0 m and  $-500$  m imply unstable stratification  
230 due to a positive heat flux (Gryning et al., 2007; Archer et al., 2016). Conversely, lengths between 0 m and 500 m  
231 imply stable stratification due to a negative heat flux. Lengths approaching negative or positive infinity imply  
232 neutral stratification, as buoyancy is no longer a dominating factor. Each 10 min timestamp from the NWF run is  
233 assigned a stability classification from November 2019 to March 2020.

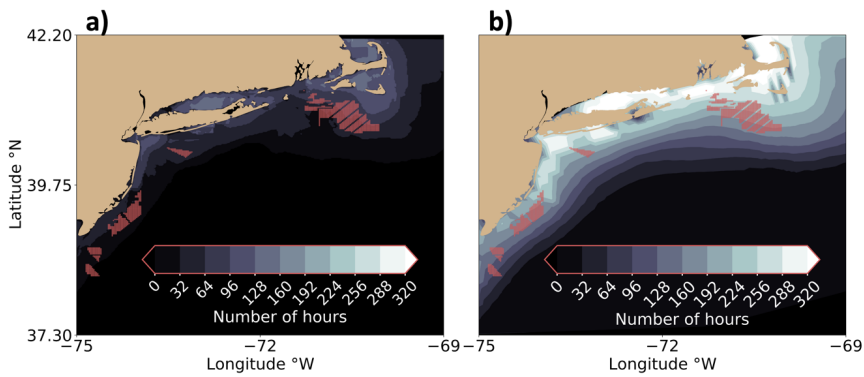
234

235 **3 Results**

236 **3.1 Spatial variability of icing conditions**

237 The prevalence of icing conditions exhibits regional variability. The commonality of icing increases toward  
238 higher latitudes and near the coast where cold continental air advects over the ocean during the winter (Figure 2). In  
239 general, the spatial icing pattern during the 2019–2020 winter season (Figure 2a) matches well with the pattern over  
240 the 21-year period (Figure 2b) although the 2019–2020 season is relatively mild compared to other winters (Figure  
241 2, Figure 3a). Icing conditions shadow the mid-Atlantic coast but occur less often along the New Jersey Bight where

242 wind speeds decrease and air and sea temperatures warm. The prevalence of freezing conditions extends furthest  
 243 offshore southeast of Nantucket and enhances in the Long Island Sound; both regions feature local minima in mean  
 244 January 2020 SST less than 5° C. The Long Island Sound is flanked by land to the north and south which amplifies  
 245 the presence of cold air. In addition, mean wind speeds maximize to the east of Cape Cod and Nantucket (Bodini et  
 246 al., 2024) which increases the number of hours that wind-generated spray is present. Finally, the cyclonic current in  
 247 the Gulf of Maine transports water southward. East of Cape Cod, this current bifurcates around the Georges Bank,  
 248 and a branch feeds cold water into the mid-Atlantic (Chapman et al., 1986). The number of icing hours may be  
 249 further exacerbated when predominant northerly winter winds instigate onshore Ekman transport toward the coast,  
 250 which is favorable for downwelling (Shcherbina and Gawarkiewicz, 2008b). However, downwelling is not always  
 251 supported, as the mixed layer stratification is dominated by salinity (Shcherbina and Gawarkiewicz, 2008a), leaving  
 252 a cold pool near the surface.  
 253



254  
 255 **Figure 2. The number of hours FSS conditions occur at 10 m during (a) the November 2019 to March 2020 period in**  
 256 **NWF and (b) the mean November to March period from 2000 to 2020 in NOW-23. Lighter contouring indicates more**  
 257 **freezing hours. Red dots represent turbine locations but do not exist in (a) or (b) and are shown for reference.**

258  
 259  
 260  
 261 Icing conditions exhibit seasonal variability in NWF, starting at 0 hours in November, increasing through the  
 262 winter, and falling to 0 again by April at all heights (Figure 3 and Figure. A1–A3). At the 10 m altitude, FSS  
 263 conditions occur most often in January, up to 67 hours, with an offshore spatial extent of 59,292 km<sup>2</sup>, or 12.3 times  
 264 the area of the wind plants. At 20 m, FSS conditions also occur most often in January, up to 68 hours, covering a  
 265 total area of 61,736 km<sup>2</sup>, or roughly 12.8 times the area of the wind plants (Figure A2). The 138 m hub height attains  
 266 the largest maximum of 119 hours during January in the Gulf of Maine and to the east Cape Cod (Figure A3), with  
 267 an offshore spatial extent of 291,012 km<sup>2</sup>, or 60.2 times the area of the wind plants.  
 268



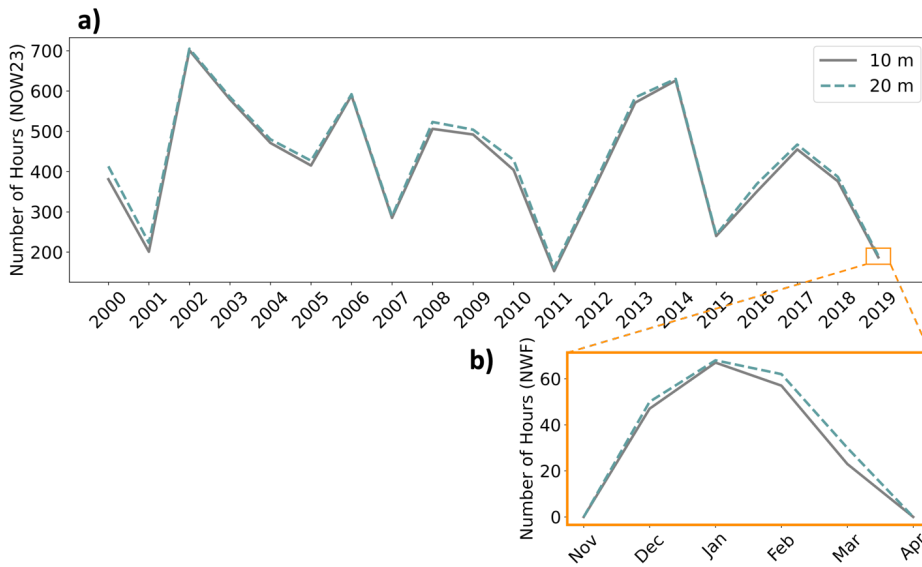


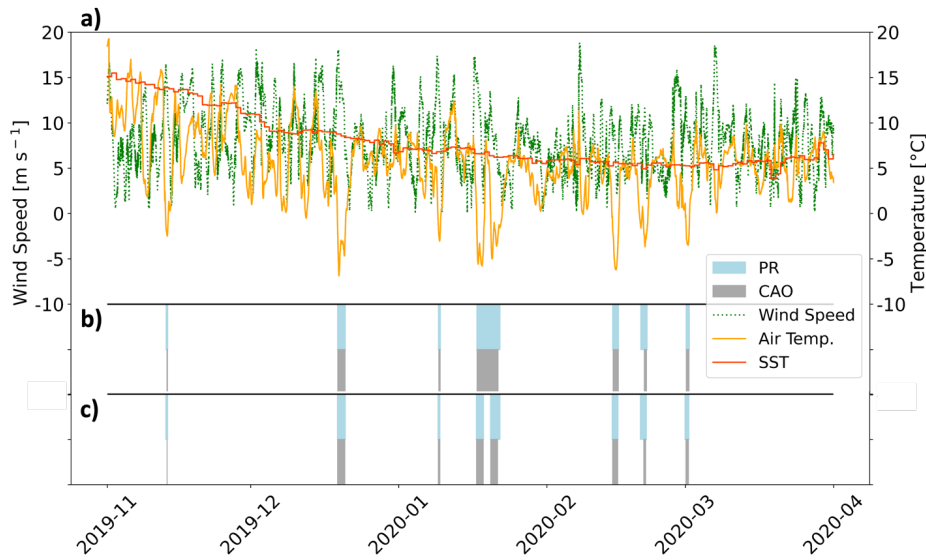
Figure 3. The maximum number of FSS hours over the OCS (a) annually and (b) seasonally in NOW-23. The zoomed orange cutout shows the seasonal variation over the 2019–2020 winter.

269  
 270  
 271  
 272  
 273 The 2019–2020 winter season was one of the mildest compared to other winters (Figure 3a), as assessed using  
 274 the FSS detection criteria (Section 2.3). This winter season had few icing hours compared to other winters over the  
 275 21-year period, reaching 194 hours in NWF or 187 hours in NOW-23 at 10 m. At 20 m, the 2019–2020 winter  
 276 season contains 210 hours in NWF or 191 hours in NOW-23. The greatest number of icing hours occurs during the  
 277 2002–2003 season, with 701 total hours at 10 m and 705 hours at 20 m. While the 21-year slope shows a decrease, it  
 278 is not statistically significant using the Mann–Kendall (M–K) test (Hussain and Mahmud, 2019). P-values for the  
 279 maximum number of icing hours (found across the OCS) (Figure 3a) and for the number of hours at the POI (Figure  
 280 1) are 0.20 and 0.12, respectively. We additionally applied the seasonal M–K test (Hirsch et al., 1982) to account for  
 281 upward and downward trends throughout the year on monthly mean PR, monthly maximum PR, and the monthly  
 282 total number of icing hours at the POI. Neither test returned a statistically significant trend.

### 283 3.2 Icing conditions and cold air outbreak

284  
 285 Investigating all events with a non-zero PR at the POI (Figure 1) reveals similar synoptic trends. We identify  
 286 seven events with FSS conditions with a total duration of 253 hours from November 2019 to March 2020. All times  
 287 during the 2019–2020 winter period with nonzero PR contain light ice accumulation of less than  $0.7 \text{ cm h}^{-1}$  (Table  
 288 2). During each FSS event, higher relative pressure resided to the southwest throughout the Great Plains,  
 289 Appalachia, or the Great Lakes with lower relative pressure to the northeast around Nova Scotia and

290 Newfoundland. In the Northern Hemisphere, winds flow with higher pressure to the right and lower pressure to the  
 291 left (Wallace and Hobbs, 2006). This flow regime results from the balance between the pressure gradient force and  
 292 the Coriolis force, which is a force introduced into the equations of motion to account for acceleration on a non-  
 293 inertial rotating reference frame (Ferrel, 1856). The largest pressure gradient forces occurred during the two January  
 294 events reaching 4 hPa per 100 km, or roughly 4 times the pressure gradient force required for a 10 m s<sup>-1</sup> geostrophic  
 295 wind in the midlatitudes. Most events feature a cold front in the mid-Atlantic. This pressure regime directs quasi-  
 296 geostrophic flow near the surface toward the southeast, introducing cold continental air offshore. During the winter,  
 297 the prevailing wind direction is northwesterly across the mid-Atlantic OCS (Bodini et al., 2019) because regions of  
 298 land mass feature higher surface pressure than the surrounding ocean and the Bermuda High retreats to the east.  
 299



300 **Figure 4. (a) Time series of wind speed (green dotted), 10 m air temperature (orange), and SST (red) from November**  
 301 **2019 to April 2020 at the downwind edge of Vineyard Wind (Figure 1). Light-blue shading indicates the duration of**  
 302 **nonzero PR, and gray shading indicates the duration of detected CAO from (b) NWF and (c) NOW-23.**  
 303

304  
 305 All FSS events, assessed using PR, coincide with CAO. We detect seven CAO events in NWF with a total  
 306 duration of 202 hours (Figure 4b). The mean duration of CAO events (29 hours) are seven hours shorter than FSS  
 307 events (36 hours), with 80 % of flagged FSS timestamps having CAO present.  
 308

309 Common between events are fast wind speeds and cold 10 m air temperatures; SST plays a secondary role for  
 310 its weak temporal variability (Figure 4a). The average wind speed during FSS events is 10 m s<sup>-1</sup> with gusts

311 exceeding  $15 \text{ m s}^{-1}$  during four events. Nonzero PR does not occur until after the wind speed peaks, when cold air  
312 temperatures sweep in, averaging minimum temperatures of  $-4.5^\circ \text{ C}$  (Figure 4a). This wind speed–temperature  
313 dynamic can pose a challenge for grid planners if wind energy generation reduces during periods of high demand for  
314 residential and commercial heating, especially in a future scenario with electrification of space heating.

315

316 During the 2019–2020 winter in the NOW-23 dataset, eight total events are flagged as candidates for FSS  
317 because the longest event in January 2020 (Figure 4b) is split among two separate events; all eight events have a  
318 corresponding CAO (Figure 4c). Over the 21-year period, *all* CAO events occur in conjunction with an FSS event  
319 (positive PR) (Fig. C1–Fig. C20). However, many FSS events occur without CAO present meaning that CAO is  
320 only one of the drivers, and large interannual variability can exist. For instance, while 100 % of CAO timestamps  
321 concur with FSS during the 2011–2012 season, only 10 % do during the 2013–2014 season.

322

323 The 2019–2020 winter ice accumulation rate is similar to other winters. The average PR during freezing events  
324 from 2019 to 2020 is 4.3, which corresponds to a light ice accumulation rate of less than  $0.7 \text{ cm h}^{-1}$  (Table 2). Over  
325 the 21-year period, the average PR among events is 8.1, which corresponds to the same accumulation rate. The  
326 2003–2004 winter period features the greatest mean PR of 15.7, which also corresponds to a light ice accumulation  
327 rate. During this winter, a moderate risk for icing occurred 18 % of the time, and a heavy risk occurred 3 % of the  
328 time, corresponding with icing rates between  $0.7\text{--}2.0 \text{ cm h}^{-1}$  and  $2.0\text{--}4.0 \text{ cm h}^{-1}$ , respectively, and possibly  
329 triggering heavy freezing spray watches in the NWS advisory.

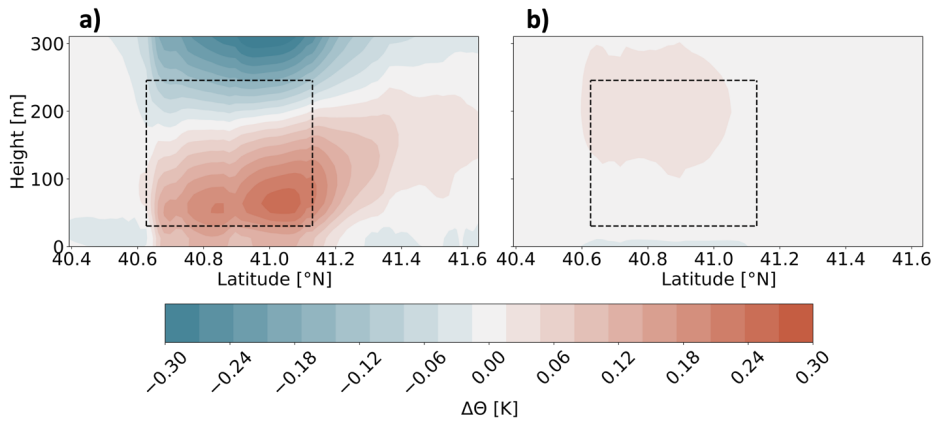
330 Synoptic-scale teleconnection patterns can impact the likelihood of icing conditions. From December 2003 to  
331 March 2004, the Pacific North Atlantic (PNA) cycle was positive. During the positive phase of PNA, a relative high-  
332 pressure anomaly with anticyclonic wind flow exists over the western US that is conducive to northwesterly  
333 transport of cold air over the East Coast (Vavrus et al., 2006). In addition, the entire November 2003 to March 2004  
334 period featured a positive El Niño–Southern Oscillation (ENSO) index. Positive ENSO has been attributed to cooler  
335 SSTs across the mid-Atlantic and northeasterly winds which advect cold air from the north (Alexander and Scott,  
336 2002). Other teleconnection patterns, including the Arctic Oscillation and North-Atlantic Oscillation switched signs  
337 during this winter and are not discussed in greater detail.

338

### 339 **3.3 Modifications by wind plants**

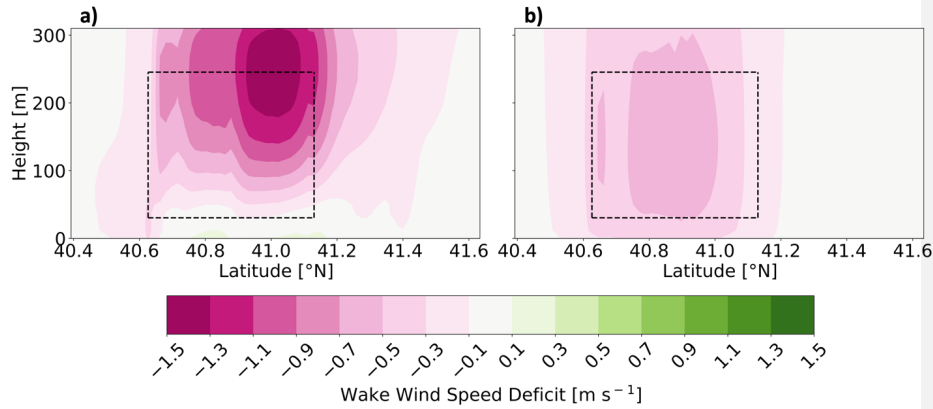
340 The near-surface cooling effect by rotor turbulence provides a subtle effect on freezing conditions. In unstable  
341 conditions, which occur 64 % of the time from November 2019 through March 2020 in NWF assessed at the POI,  
342 wind turbines introduce near-surface cooling, which could increase the likelihood of freezing. Mean cooling and  
343 warming during unstable conditions reach magnitudes up to  $-0.041 \text{ K}$  at the surface and  $0.022 \text{ K}$  within the rotor-  
344 swept region, respectively, along a cross section extending through the RIMA block (Figure 1, Figure 5b). During  
345 stable conditions, which occur 25 % of the time from November through March, cooling aloft reaches up to  $-0.34$   
346 K, and near-surface warming reaches  $0.26 \text{ K}$  (Figure 5a). Near-surface cooling exists adjacent to the wind plant  
347 cluster (Xia et al., 2016).

348



349 **Figure 5. The mean (WFP-NWF) potential temperature difference during (a) stable stratification and (b) unstable**  
 350 **stratification, from November 2019 to March 2020. The cross section spans the RIMA block of lease areas (Figure 1). Red**  
 351 **contouring indicates warming, and blue indicates cooling. Dashed lines outline the wind plant area and rotor-swept**  
 352 **region.**  
 353

354  
 355 The reduction of wind speeds in the wake modifies the chance for icing within the rotor-swept area and near the  
 356 surface by reducing the production of white-capped waves and the wind-induced tearing of spray off waves. In  
 357 stable conditions, the mean wake wind speed deficit is largest, reaching  $-1.4 \text{ m s}^{-1}$  near the top of the rotor-swept  
 358 plane, reducing the chance for icing. Because vertical motion is suppressed in stable stratification, winds enhance  
 359 and flow around and under the wind plant area (Figure 6a), reaching a subtle enhancement near the surface of  $0.18$   
 360  $\text{m s}^{-1}$ . In unstable stratification, available buoyant turbulence promotes mixing which transports momentum from  
 361 above the rotor-swept region down to within the wake. The injection of momentum allows wake wind speeds to  
 362 recover, leaving a smaller maximum averaged wake deficit of  $-0.57 \text{ m s}^{-1}$  (Figure 6b). There is no enhancement of  
 363 wind speeds adjacent to the RIMA block along the cross section in unstable conditions.  
 364



365  
 366 **Figure 6. The mean (WFP-NWF) wind speed difference during (a) stable and (b) unstable stratification, from November**  
 367 **2019 to March 2020. The cross section spans the RIMA block of lease areas (Figure 1). Pink contouring indicates a wind**  
 368 **speed reduction, and green indicates wind speed enhancement. Dashed lines outline the wind plant area and rotor-swept**  
 369 **region. Note the very small enhancement of wind speeds near the surface in stable conditions.**

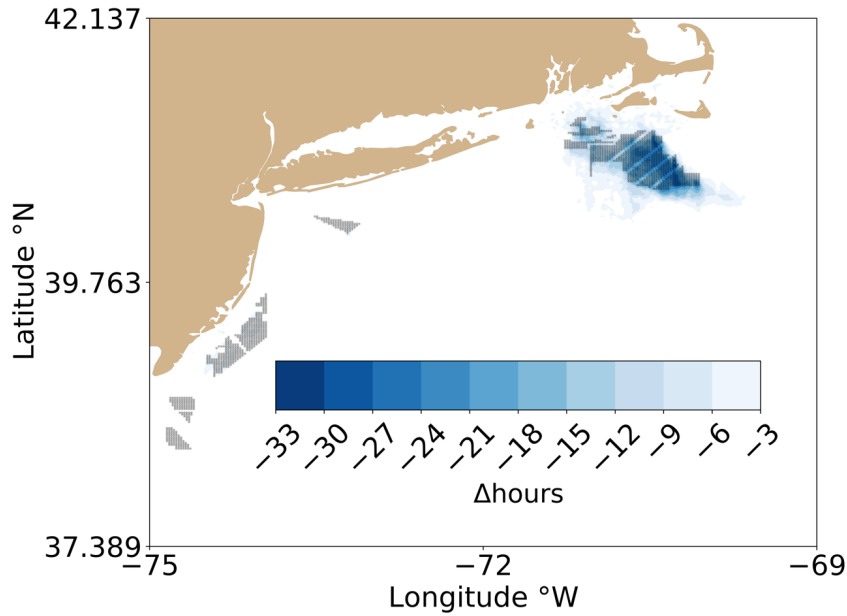
370  
 371 Despite near-surface cooling, net FSS conditions in WFP occur less often than in NWF when diagnosed using  
 372 wind speed, air temperature, and SST criteria because of the wake wind speed reduction. At 10 m, the turbine–  
 373 atmosphere interaction alters possible icing conditions the most in February, with a maximum reduction by 15 hours  
 374 (Table 3). At 20 m, wind plants cause a reduction by up to 15 hours in January and February. In each case, the  
 375 reduction in possible icing conditions is spatially coincident with the wind plant areas (Figure 7). At the 138 m hub  
 376 height, the change to the number of FSS hours also maximizes in January and February, with a reduction by 9 hours.  
 377

378 **Table 3. The maximum turbine-induced change in FSS hours by month and height.**

	November	December	January	February	March	April
10 m	0	-3	-14	-15	-11	0
20 m	0	-4	-15	-15	-12	0
138 m	0	-5	-9	-9	-5	0

379

380



381

382 **Figure 7. The (WFP-NWF) change in number of FSS hours at 10 m November 2019 to March 2020. Blue contours**  
383 **indicate a reduction.**

383

384

385

386 Similarly, the presence of wind turbines has a minimal impact to the number of hours FSS conditions occur by  
387 means of icing PR at the POI. The duration of nonzero PR over the November through March winter period  
388 increases by 3 hours, or from 253 to 256 hours total, at a point centered on the RIMA block. The total duration of  
389 CAO does not change after the installation of wind plants and remains at 202 hours. The total number of events  
390 (seven) does not change in the presence of wind turbines, and all flagged timestamps still cause light icing of less  
391 than  $0.7 \text{ cm h}^{-1}$ .

391

392

#### 4 Conclusions

393

394 Herein, we assess the threat of icing conditions at 10 and 20 m due to freezing sea-spray and at the hub height  
395 due to precipitation and in-cloud icing. The simulation study encompasses the mid-Atlantic Outer Continental Shelf  
396 based on a 21-year WRF dataset from 01 January 2000 to 31 December 2020 and another WRF dataset using year-  
397 long simulations from 01 September 2019 to 31 August 2020. In each case, we focus on the wintertime period from  
398 November through March. We consider the present icing risk from simulations with no wind farms (NOW-23,  
399 NWF) and assess the post-construction adjustments by incorporating the effects of turbines (WFP) in a full buildout  
of the wind plant lease areas.

399

400  
401 Using an FSS predictability equation (PR), we detect seven events flagged for FSS conditions in NWF with a  
402 total duration of 253 hours during the November 2019 to March 2020 period. All times during the period with  
403 nonzero icing predictability (PR) contain light ice accumulation of less than  $0.7 \text{ cm h}^{-1}$ , which is typical of the mid-  
404 Atlantic bight as assessed from 2000 to 2020. Centered at the RIMA block of lease areas, all seven events have an  
405 associated CAO during the 2019–2020 winter. In the NOW-23 dataset from November 2019 to March 2020, eight  
406 total events are flagged, and all eight correspond with CAO. Over the 21-year climatology, every CAO event has a  
407 corresponding FSS event, although not all FSS events have attendant CAO. Thus, offshore icing conditions may be  
408 forecast with reasonable fidelity through accompanying CAO, although other drivers exist. There is strong  
409 teleconnection between anomalous arctic sea level pressure sea level pressure and CAO, as 93 % of CAO events in  
410 the eastern U.S. contained an antecedent positive arctic sea level pressure anomaly a week in advance (Vavrus et al.,  
411 2006).

412  
413 The number of FSS hours exhibit spatial variability, as assessed using our detection criteria of low air sea  
414 surface temperatures and strong winds . The hazards intensify toward higher latitudes where air and sea  
415 temperatures are colder and wind speeds are faster, near the land surface where cold air advects offshore, and by  
416 Nantucket and the Long Island Sound where SSTs are colder. Icing conditions at the hub height, as assessed by low  
417 air temperatures and precipitation or saturated air, are more frequent. The icing hazard is greatest during January  
418 when wind speeds are fast and temperatures are cold. At 10 m in January, favorable conditions for icing occur up to  
419 67 hours. At 20 m in January, the duration of icing conditions is similar at 68 hours. Finally, at the hub height, icing  
420 conditions occur for up to 119 hours east of Cape Cod. Overall, the 2019–2020 winter period is the mildest winter  
421 when considering the 21-year climatology. Although the 2019–2020 winter season has the fewest number of  
422 freezing sea spray hours, all winters contain light ice accumulation rates of  $0.7 \text{ cm h}^{-1}$ .

423  
424 The introduction of large wind plants makes a small impact on the icing risk within the wind plant clusters. In  
425 wintertime unstable conditions, which occur 64 % of the time from November 2019 through March 2020, wind  
426 turbines introduce a mean near-surface cooling effect. Despite the enhanced freezing risk from supplementary  
427 cooling, slower wind speeds in the wake mitigate the icing hazard. A mean reduction in wind speeds within wakes  
428 reaches up to  $-0.57 \text{ m s}^{-1}$  in unstable stratification with a mean introduction of cooler air up to  $-0.041 \text{ K}$ . As  
429 assessed using wind speed, air temperature, and SST criteria, the change in FSS risk over the 2019–2020 wintertime  
430 period is a net reduction, by only 15 hours at both 10 and 20 m. The alleviation by slower wind speeds is largest  
431 within the RIMA block of wind plants which contains the greatest number of turbines and the greatest number of  
432 FSS hours relative to other wind energy areas. When assessed using PR centered on the RIMA block, the number of  
433 icing hours increases by 3 with no change to CAO hours. Although the 2019 through 2020 winter period is the  
434 mildest winter, and thus not representative of the 21-year climatology of FSS conditions, this period captures well  
435 the post-construction effects of wind plants. We note that such effects may be more significant during during harsher  
436 winters.

437

438 Future OCS winter storm frequency may differ due to climate change. For instance, warming Arctic  
439 temperatures, which reduce the meridional geopotential height gradient between the Arctic and midlatitudes, can  
440 weaken the jet stream. Slower zonal winds and more pronounced Rossby waves amplify the transport of extreme  
441 winter weather to the midlatitudes (Cohen et al., 2020). Future East Coast storm activity and temperature may  
442 experience modulations based on large-scale teleconnections such as El Niño and the North Atlantic Oscillation  
443 (Hall and Booth, 2017). Further, Arctic amplification may increase the strength of teleconnection found between  
444 positive Arctic sea level pressure anomalies and CAO (Vavrus et al., 2006).

445

446 Finally, we assume that sea spray provides a consistent moisture flux at 10 and 20 m during fast wind  
447 conditions, that the droplet size of spray is homogeneous, and that the number distribution by height is constant. The  
448 impingement of waves onto offshore structures provides a larger source of moisture than wind-generated spray that  
449 is dependent on the wave height and wave period. Future studies may benefit from coupling WRF with wave  
450 models, such as Wave Watch III (Tolman et al., 2019) and Simulating WAVes Nearshore (SWAN Team, 2020) for  
451 precise modeling of wave characteristics and current dynamics, such as stratified cold pooling around Cape Cod.  
452 New satellite methods are being developed to quantify occurrences of freezing sea spray (Line et al., 2022), and  
453 future developments could compare the FSS criteria to satellite observations of FSS.

454

#### 455 **5 Code and data availability**

456 The dataset and files that support this work are publicly available. The ERA5 initial and boundary conditions can be  
457 downloaded from the ECMWF Climate Data Store at [https://cds.climate.copernicus.eu/cdsapp#!/dataset/reanalysis-  
era5-pressure-levels?tab=form](https://cds.climate.copernicus.eu/cdsapp#!/dataset/reanalysis-era5-pressure-levels?tab=form). Shapefiles including the bounds for wind energy lease areas are at  
458 <https://www.boem.gov/renewable-energy/mapping-and-data/renewable-energy-gis-data>. Wind turbine coordinates  
459 and their power and thrust curves are provided at <https://zenodo.org/record/7374283#.Y4YZxC-B1KM>. WRF  
460 namelists for NWF and WFP simulations may be acquired from [https://zenodo.org/record/7374239#.Y4YaOy-  
B1KM](https://zenodo.org/record/7374239#.Y4YaOy-B1KM). The NOW-23 simulation output data are available in HDF5 format at <https://doi.org/10.25984/1821404>.

463

#### 464 **6 Author contributions**

465 Conceptualization: JKL. Resources: MO, NB. Methodology: DR, JKL. Software: DR. Formal analysis and  
466 visualization: DR. Investigation: DR and JKL. Writing – original draft: DR and JKL. Writing – review and editing:  
467 all co-authors. Supervision: JKL.

468

#### 469 **7 Competing interests**

470 At least one of the (co-)authors is a member of the editorial board of Wind Energy Science. Furthermore, Mike  
471 Optis co-authored the submitted manuscript while an employee of the National Renewable Energy Laboratory. He  
472 has since founded Veer Renewables, which recently released a wind modeling product, WakeMap, which is based  
473 on a similar numerical weather prediction modeling framework as the one described in this manuscript. Data from  
474 WakeMap is sold to wind energy stakeholders for profit. Public content on WakeMap include a website (htt



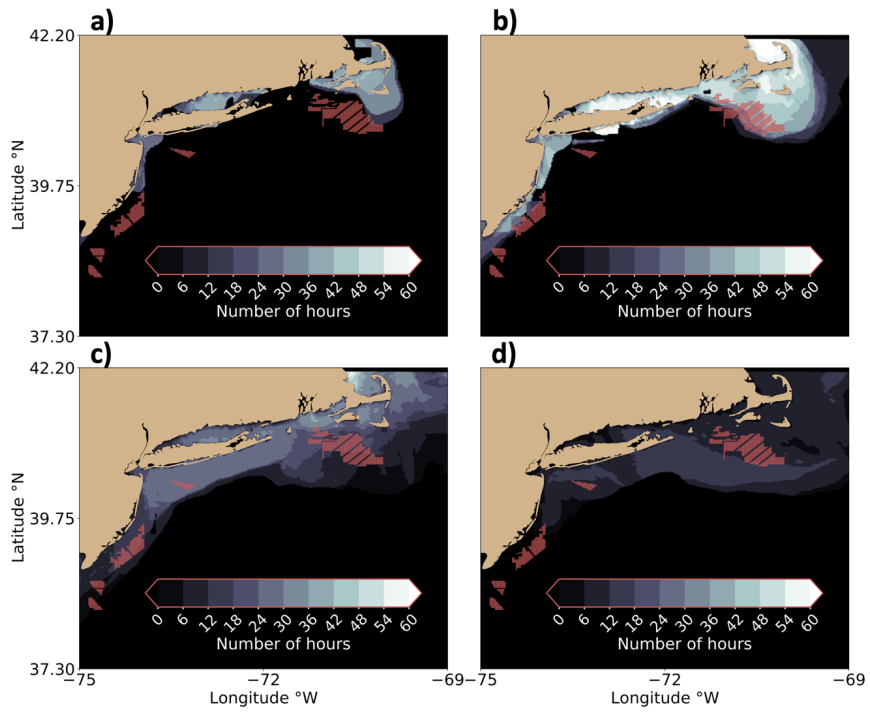
475 J.Mps://veer.eco/wakemap/), a white paper (<https://veer.eco/wp->  
476 [content/uploads/2023/02/WakeMap\\_White\\_Paper\\_Veer\\_Renewables.pdf](https://veer.eco/wp-content/uploads/2023/02/WakeMap_White_Paper_Veer_Renewables.pdf)) and several LinkedIn posts promoting  
477 WakeMap. Mike Optis is the founder and president of Veer Renewables, a for-profit consulting company. Mike  
478 Optis is a shareholder of Veer Renewables and owns 92 % of its stock.

479  
480 **8 Acknowledgements**

481 This work utilized the Alpine high-performance computing resource at the University of Colorado Boulder. Alpine  
482 is jointly funded by the University of Colorado Boulder, the University of Colorado Anschutz, and Colorado State  
483 University. Data storage supported by the University of Colorado Boulder ‘PetaLibrary’ A portion of this research  
484 was performed using computational resources sponsored by the DOE’s Office of Energy Efficiency and Renewable  
485 Energy and located at NREL. This work was authored in part by the National Renewable Energy Laboratory,  
486 operated by Alliance for Sustainable Energy, LLC, for the US Department of Energy (DOE) under contract no. DE-  
487 AC36-08GO28308. Funding was provided by the US Department of Energy Office of Energy Efficiency and  
488 Renewable Energy Wind Energy Technologies Office. Support for the work was also provided by the National  
489 Offshore Wind Research and Development Consortium under agreement no. CRD-19-16351. The views expressed  
490 in the article do not necessarily represent the views of the DOE or the US Government. The US Government retains  
491 and the publisher, by accepting the article for publication, acknowledges that the US Government retains a  
492 nonexclusive, paid-up, irrevocable, worldwide license to publish or reproduce the published form of this work, or  
493 allow others to do so, for US Government purposes.

494 The authors wish to thank Louis Bowers and Sarah McElman for their questions that led to this line of inquiry.

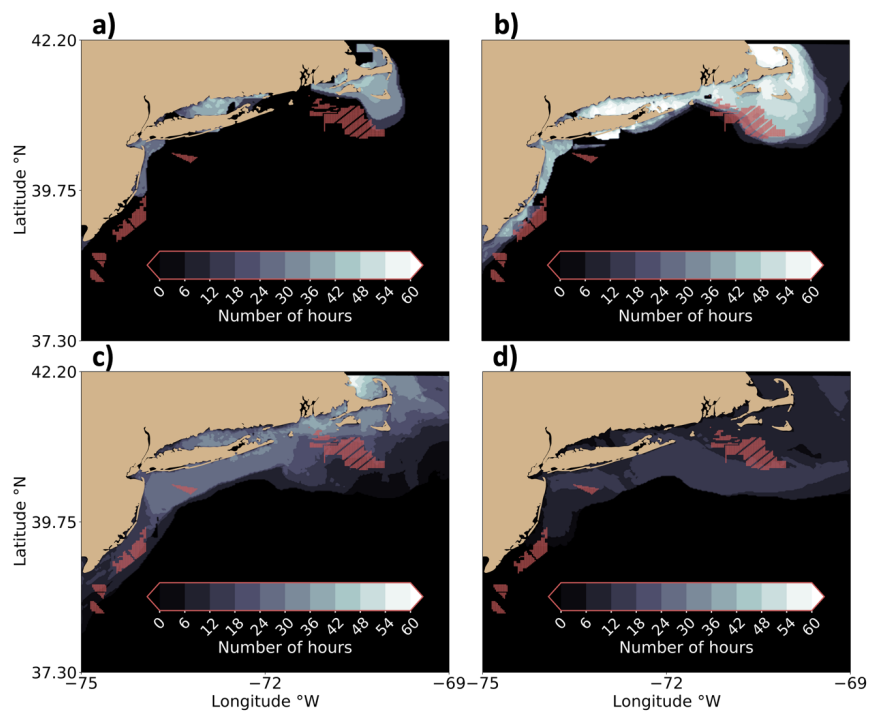
495  
496 **9 Appendices**  
497 **Appendix A**



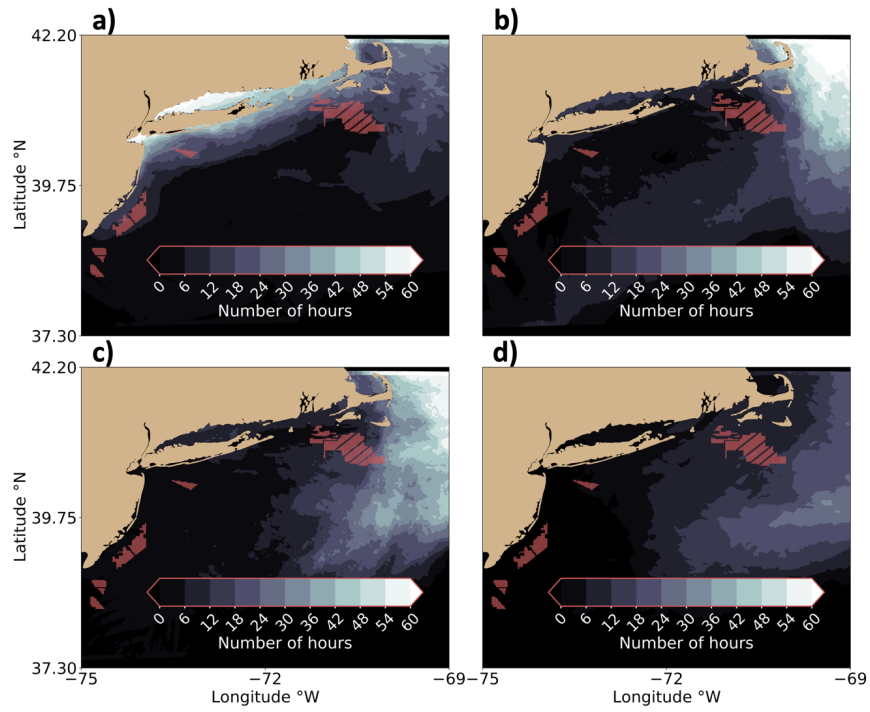
498

499 **Figure. A1. The number of freezing hours at 10 m during (a) December 2019, (b) January 2020, (c) February 2020, and**  
 500 **(d) March 2020. Lighter contouring indicates higher percentages. Red dots indicate turbine locations.**

501



502  
 503 **Figure A2.** The number of freezing hours at 20 m during (a) December 2019, (b) January 2020, (c) February 2020, and (d)  
 504 **March 2020.** Lighter contouring indicates higher percentages. Red dots indicate turbine locations.  
 505



506

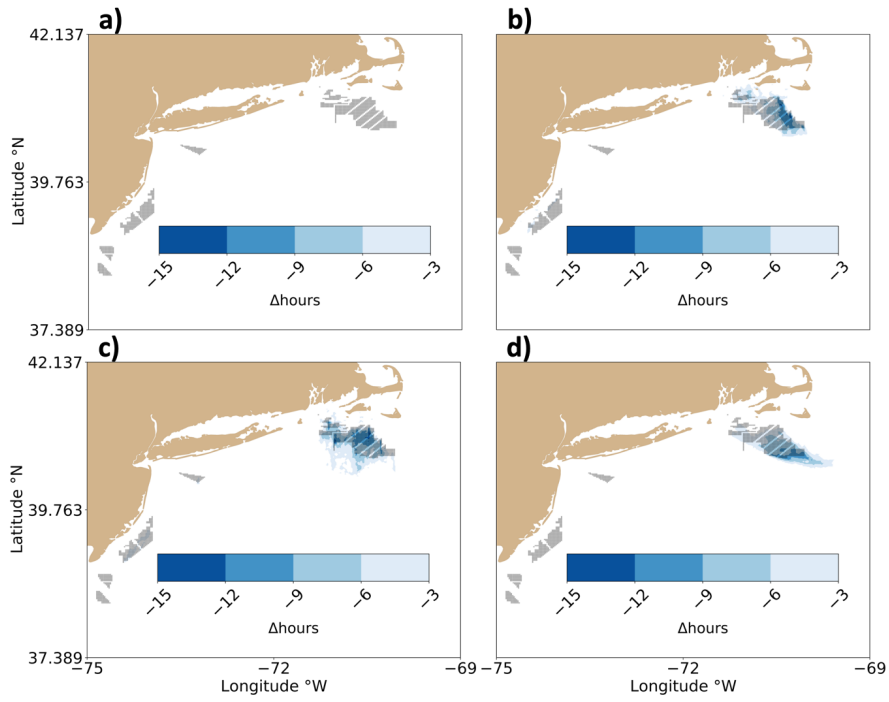
507

508

509

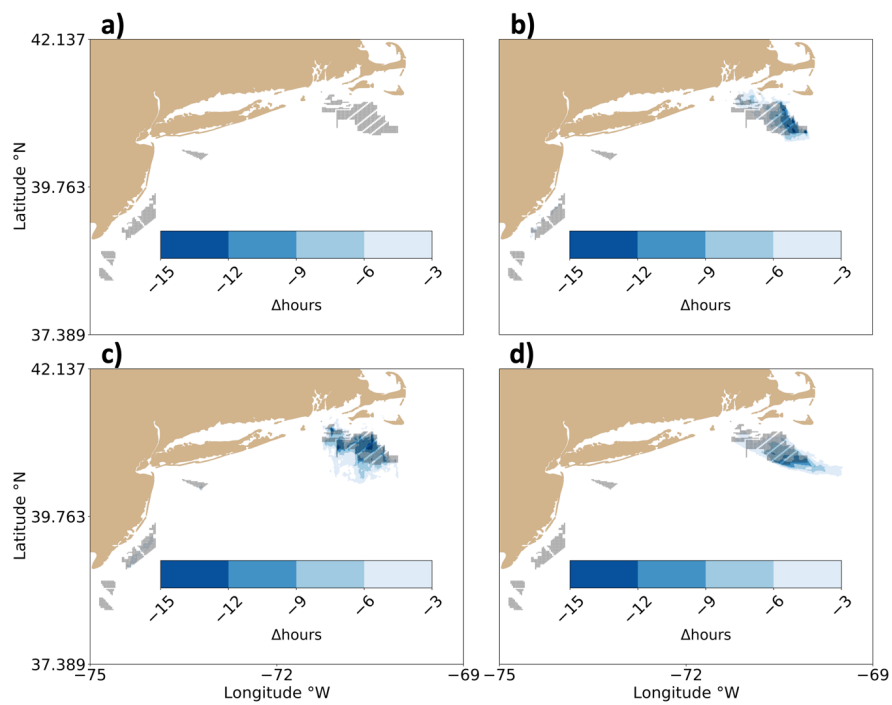
Figure A3. The number of freezing hours at hub height during (a) December 2019, (b) January 2020, (c) February 2020, and (d) March 2020. Lighter contouring indicates higher percentages. Note the color scheme is different from Supplementary Figs. 1 and 2. Red dots indicate turbine locations.

510



511  
 512 **Figure A4.** The (WFP-NWF) difference in freezing hours at 10 m during (a) December 2019, (b) January 2020, (c)  
 513 February 2020, and (d) March 2020. Blue contouring indicates fewer hours. Gray dots indicate turbine locations.

514



515  
 516 **Figure A5. The (WFP\_0-NWF) difference in freezing hours at 20 m during (a) December 2019, (b) January 2020, (c)**  
 517 **February 2020, and (d) March 2020. Blue contouring indicates fewer hours. Gray dots indicate turbine locations.**

518

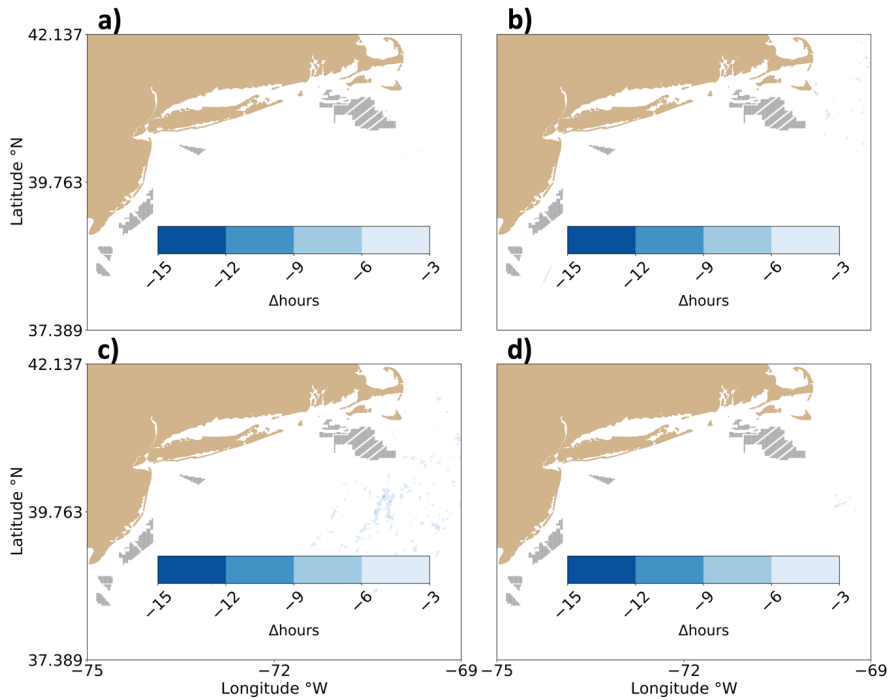


Figure A6. The (WFP-NWF) difference in freezing hours at the hub height during (a) December 2019, (b) January 2020, (c) February 2020, and (d) March 2020. Blue contouring indicates fewer hours. Gray dots indicate turbine locations.

519  
520  
521

522 **Appendix B**

523 As discussed in Section 2.3, we detect FSS conditions using common thresholds for the meteorological  
524 conditions (Guest and Luke, 2005; Dehghani-Sanij et al., 2017; Line et al., 2022). These criteria require strong wind  
525 speeds greater than  $9 \text{ m s}^{-1}$ , cold air temperatures below  $-1.7^\circ \text{C}$ , and cold SSTs less than  $7^\circ \text{C}$ . As reviewed by  
526 Dehghani-Sanij et al., (2017), FSS conditions are promising when the air temperature is below either  $-1.7^\circ \text{C}$  or  $-2^\circ$   
527  $\text{C}$  to account for the lower freezing point of saline ocean water; the salt content of which determines this threshold.  
528 Although SST thresholds of  $5^\circ \text{C}$  or  $7^\circ \text{C}$  are prevalent, a threshold up to  $8.9^\circ \text{C}$  has been used (U.S. Navy, 1988).

529 Although these thresholds were derived from observations aboard ships, the observations are sparse and have not  
530 been validated in the mid-Atlantic. Using higher air and sea surface temperature thresholds may cause an  
531 overestimation of the number of freezing hours when mid-Atlantic waters are more saline, for example, during  
532 periods with higher evaporation rates. Further, large water droplets have a higher chance of becoming runoff instead  
533 of freezing. Thus, our results may overestimate the number of icing hours where significant wave breaking and  
534 bubble bursting occur and underestimate the number of icing hours in calmer waters. As such, we quantify some of  
535 the uncertainty by calculating the number of hours that FSS conditions occur using conservative thresholds, which  
536

Formatted: Font color: Text 1

537 produce fewer icing hours (FEWER), and liberal thresholds, which promote more icing hours (MORE) (Table B1).  
 538 As there is wider agreement regarding the wind speed threshold (Dehghani-Sanij et al., 2017; Guest and Luke, 2005;  
 539 Line et al., 2022; Ross and Cardone, 1974; Monahan et al., 1983; Monahan and MacNiocaill, 1986), we hold it  
 540 constant. Due to computational constraints, we only assess the number of icing hours throughout the domain at 10 m  
 541 and during January 2020 because it has the greatest number of icing hours.

542  
 543

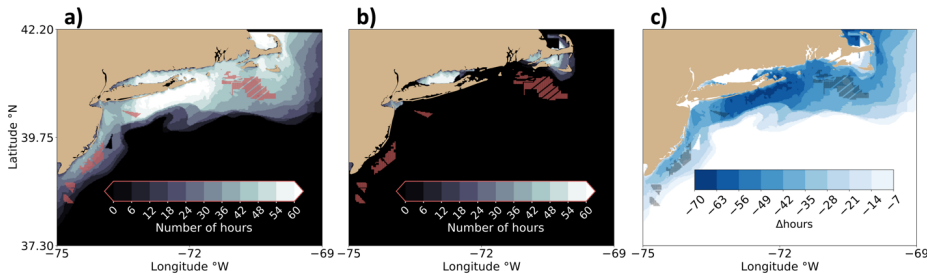
**Table B1. Icing detection criteria by sensitivity analysis type.**

Acronym	Air temperature	Sea surface temperature	Wind speed
FEWER	<-2° C	<5° C	>9 m s <sup>-1</sup>
MORE	<-1.7° C	<8.9° C	>9 m s <sup>-1</sup>

544

545 As expected, more conservative thresholds produce fewer FSS hours and vice versa (Fig. B1a,b,c). In  
 546 FEWER, the meteorological conditions conducive to icing maximize at 60 hours. Using more liberal criteria in  
 547 MORE, the maximum number of hours increases to 67. Despite the small change in the maximum number of hours  
 548 FSS occurs, the regional variation is large; the area covered by icing conditions increases from 8,924 km<sup>2</sup> to 135,244  
 549 km<sup>2</sup> from FEWER to MORE, or roughly 15 times greater than FEWER, or 2.2 times greater than our production set  
 550 of criteria. Regional variability follows SST patterns and only occurs in FEWER where the SST is relatively cold in  
 551 the Long Island Sound and Nantucket Sound (Table B1b), as discussed previously.

552



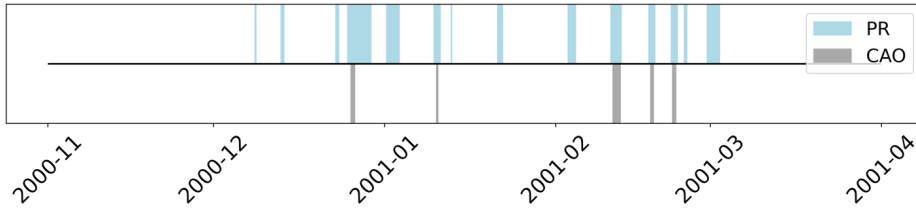
553

554 **Fig. B1. The number of hours FSS conditions occur during January 2020 at 10 m in NWF using thresholds for (a)**  
 555 **FEWER, (b) MORE, and (c) the (FEWER-MORE) difference. Lighter contouring indicates more freezing hours in (a)**  
 556 **and (b). Darker blues represent a larger reduction in number of hours in (c). Turbine locations are shown as red dots in**  
 557 **(a) and (b) and as black dots in (c).**

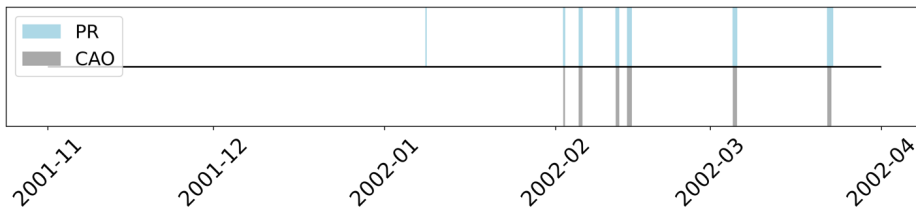
558

559 Appendix C

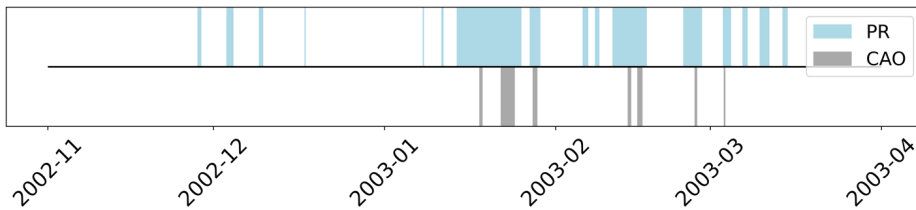




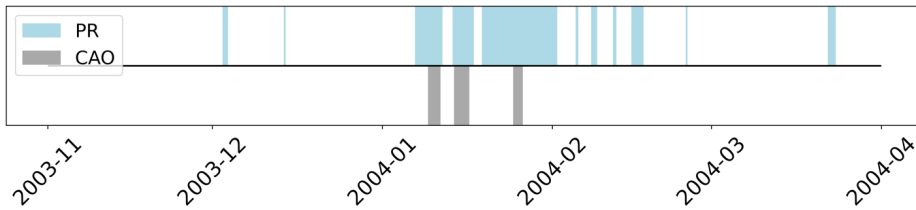
560  
561  
562 Fig. C1. Time series of CAO and FSS events from November 2000 to April 2001. Light-blue shading indicates the duration of nonzero PR and gray shading indicates the duration of detected CAO from NOW-23.



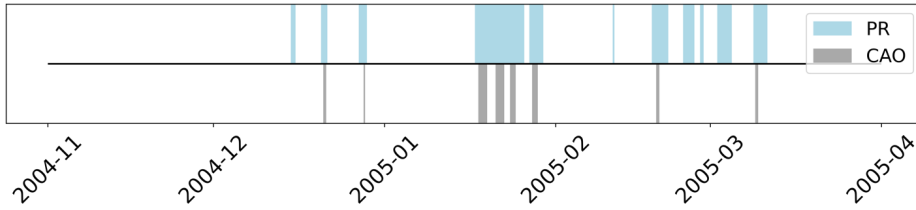
563  
564  
565 Fig. C2. Time series of CAO and FSS events from November 2001 to April 2002. Light-blue shading indicates the duration of nonzero PR and gray shading indicates the duration of detected CAO from NOW-23.



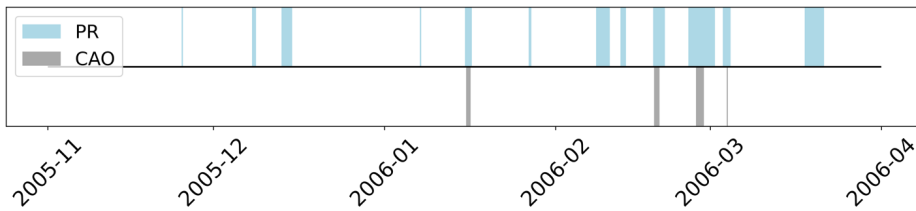
566  
567  
568 Fig. C3. Time series of CAO and FSS events from November 2002 to April 2003. Light-blue shading indicates the duration of nonzero PR and gray shading indicates the duration of detected CAO from NOW-23.



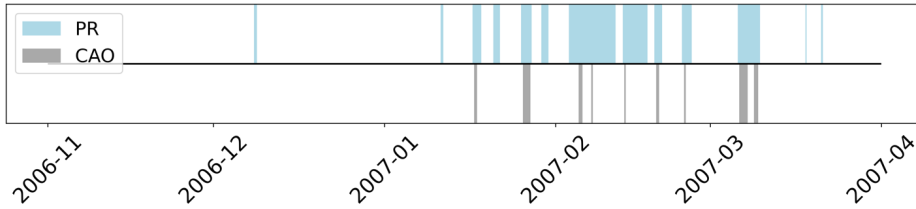
569  
570  
571 Fig. C4. Time series of CAO and FSS events from November 2003 to April 2004. Light-blue shading indicates the duration of nonzero PR and gray shading indicates the duration of detected CAO from NOW-23.



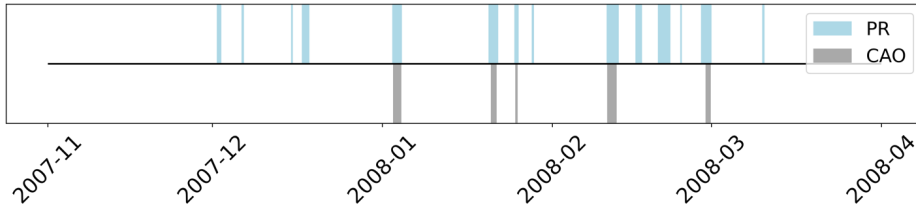
572  
573  
574 Fig. C5. Time series of CAO and FSS events from November 2004 to April 2005. Light-blue shading indicates the duration of nonzero PR and gray shading indicates the duration of detected CAO from NOW-23.



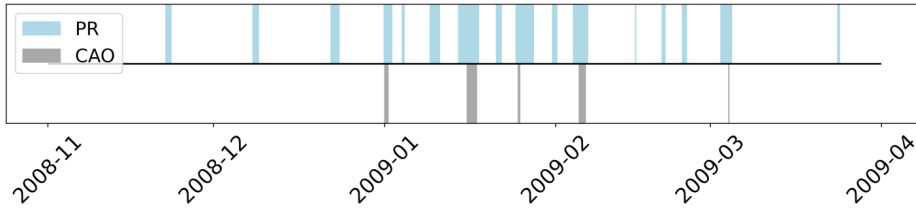
575  
576  
577 Fig. C6. Time series of CAO and FSS events from November 2005 to April 2006. Light-blue shading indicates the duration of nonzero PR and gray shading indicates the duration of detected CAO from NOW-23.



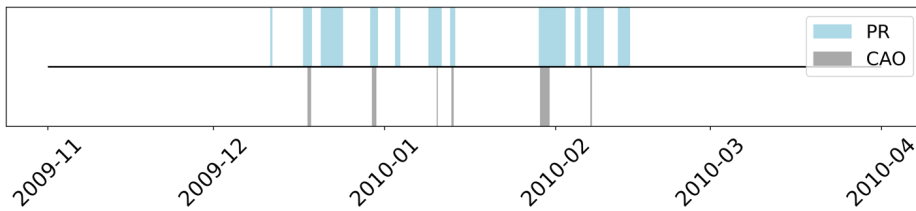
578  
579  
580 Fig. C7. Time series of CAO and FSS events from November 2006 to April 2007. Light-blue shading indicates the duration of nonzero PR and gray shading indicates the duration of detected CAO from NOW-23.



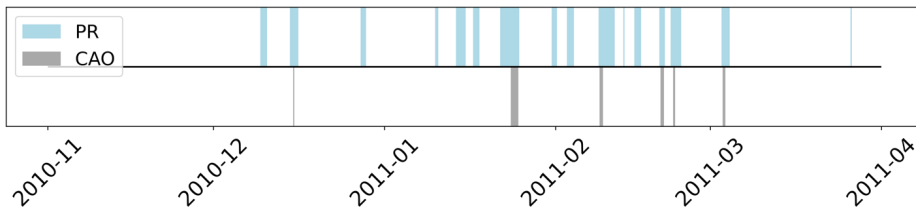
581  
582  
583 Fig. C8. Time series of CAO and FSS events from November 2007 to April 2008. Light-blue shading indicates the duration of nonzero PR and gray shading indicates the duration of detected CAO from NOW-23.



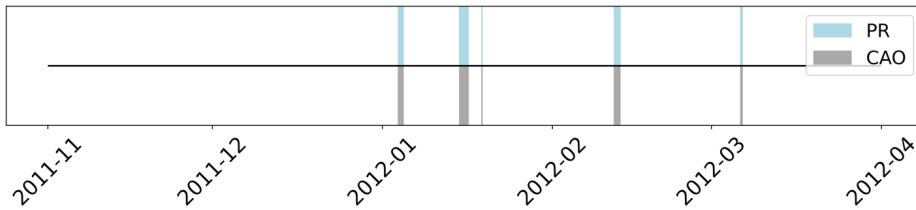
584  
585  
586 Fig. C9. Time series of CAO and FSS events from November 2008 to April 2009. Light-blue shading indicates the duration of nonzero PR and gray shading indicates the duration of detected CAO from NOW-23.



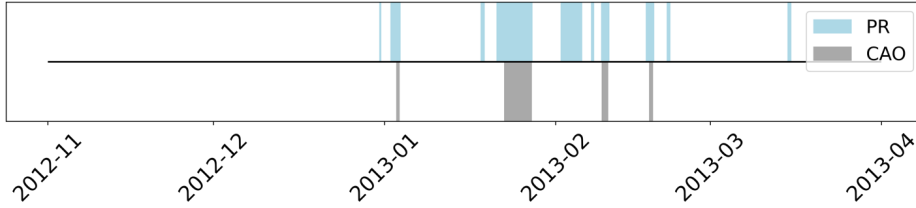
587  
588  
589 Fig. C10. Time series of CAO and FSS events from November 2009 to April 2010. Light-blue shading indicates the duration of nonzero PR and gray shading indicates the duration of detected CAO from NOW-23.



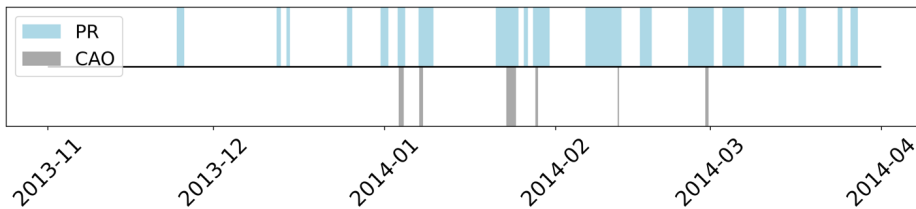
590  
591  
592 Fig. C11. Time series of CAO and FSS events from November 2010 to April 2011. Light-blue shading indicates the duration of nonzero PR and gray shading indicates the duration of detected CAO from NOW-23.



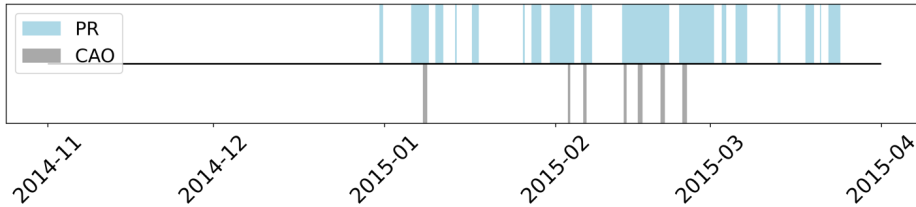
593  
594  
595 Fig. C12. Time series of CAO and FSS events from November 2011 to April 2012. Light-blue shading indicates the duration of nonzero PR and gray shading indicates the duration of detected CAO from NOW-23.



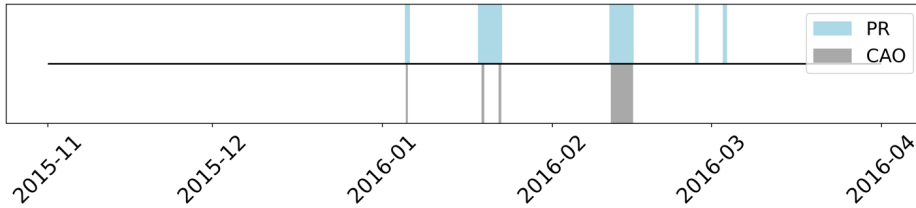
596  
597  
598 Fig. C13. Time series of CAO and FSS events from November 2012 to April 2013. Light-blue shading indicates the duration of nonzero PR and gray shading indicates the duration of detected CAO from NOW-23.



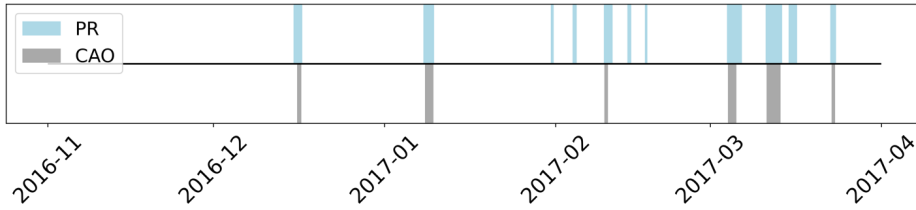
599  
600  
601 Fig. C14. Time series of CAO and FSS events from November 2013 to April 2014. Light-blue shading indicates the duration of nonzero PR and gray shading indicates the duration of detected CAO from NOW-23.



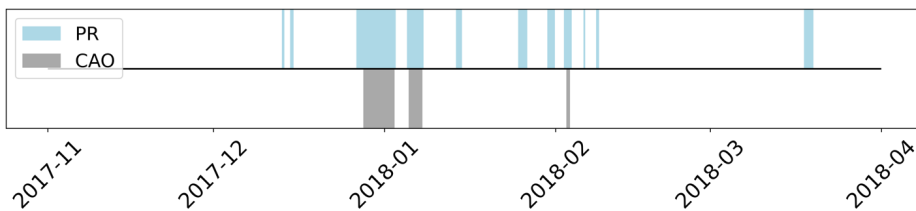
602  
603  
604 Fig. C15. Time series of CAO and FSS events from November 2014 to April 2015. Light-blue shading indicates the duration of nonzero PR and gray shading indicates the duration of detected CAO from NOW-23.



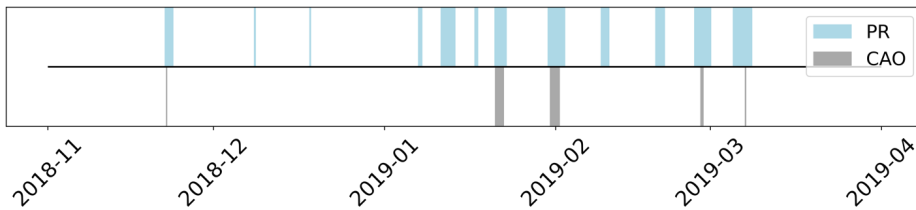
605  
606  
607 Fig. C16. Time series of CAO and FSS events from November 2015 to April 2016. Light-blue shading indicates the duration of nonzero PR and gray shading indicates the duration of detected CAO from NOW-23.



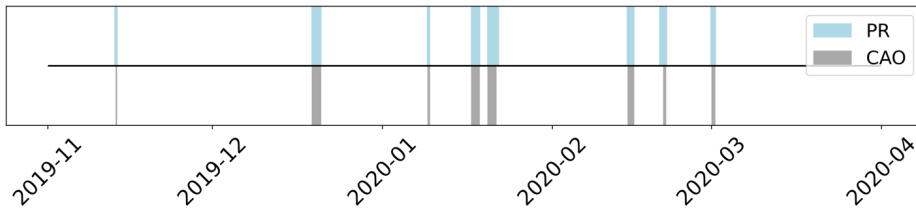
608  
609  
610 Fig. C17. Time series of CAO and FSS events from November 2016 to April 2017. Light-blue shading indicates the duration of nonzero PR and gray shading indicates the duration of detected CAO from NOW-23.



611  
612  
613 Fig. C18. Time series of CAO and FSS events from November 2017 to April 2018. Light-blue shading indicates the duration of nonzero PR and gray shading indicates the duration of detected CAO from NOW-23.



614  
615  
616 Fig. C19. Time series of CAO and FSS events from November 2018 to April 2019. Light-blue shading indicates the duration of nonzero PR and gray shading indicates the duration of detected CAO from NOW-23.



617  
618  
619 Fig. C20. Time series of CAO and FSS events from November 2019 to April 2020. Light-blue shading indicates the duration of nonzero PR and gray shading indicates the duration of detected CAO from NOW-23.

620  
621 **10 References**  
622

623 Alexander, M. and Scott, J.: The influence of ENSO on air-sea interaction in the Atlantic, Geophysical Research  
624 Letters, 29, 46-1-46-4, <https://doi.org/10.1029/2001GL014347>, 2002.

625 Archer, C. L., Colle, B. A., Veron, D. L., Veron, F., and Sienkiewicz, M. J.: On the predominance of unstable  
626 atmospheric conditions in the marine boundary layer offshore of the U.S. northeastern coast, *Journal of Geophysical*  
627 *Research: Atmospheres*, 121, 8869–8885, <https://doi.org/10.1002/2016JD024896>, 2016.

628 Archer, C. L., Wu, S., Ma, Y., and Jiménez, P. A.: Two Corrections for Turbulent Kinetic Energy Generated by  
629 Wind Farms in the WRF Model, *Monthly Weather Review*, 148, 4823–4835, [https://doi.org/10.1175/MWR-D-20-](https://doi.org/10.1175/MWR-D-20-0097.1)  
630 [0097.1](https://doi.org/10.1175/MWR-D-20-0097.1), 2020.

631 Atkinson, B. W. and Wu Zhang, J.: Mesoscale shallow convection in the atmosphere, *Reviews of Geophysics*, 34,  
632 403–431, <https://doi.org/10.1029/96RG02623>, 1996.

633 Battisti, L., Fedrizzi, R., Brighenti, A., and Laakso, T.: Sea ice and icing risk for offshore wind turbines,  
634 *Proceedings of the OWEMES*, 20–22,  
635 <https://citeseerx.ist.psu.edu/document?repid=rep1&type=pdf&doi=8bb110a8c86abf785b1b019dce37150f09de90ae>,  
636 2006.

637 Beiter, P., Musial, W., Duffy, P., Cooperman, A., Shields, M., Heimiller, D., and Optis, M.: The Cost of Floating  
638 Offshore Wind Energy in California Between 2019 and 2032, NREL/TP-5000-77384,  
639 <https://doi.org/10.2172/1710181>, 2020.

640 Bodini, N., Lundquist, J. K., and Kirincich, A.: U.S. East Coast Lidar Measurements Show Offshore Wind Turbines  
641 Will Encounter Very Low Atmospheric Turbulence, *Geophysical Research Letters*, 46, 5582–5591,  
642 <https://doi.org/10.1029/2019GL082636>, 2019.

643 Bodini, N., Optis, M., Redfern, S., Rosencrans, D., Rybchuk, A., Lundquist, J. K., Pronk, V., Castagneri, S.,  
644 Purkayastha, A., Draxl, C., Krishnamurthy, R., Young, E., Roberts, B., Rosenlieb, E., and Musial, W.: The 2023  
645 National Offshore Wind data set (NOW-23), *Earth System Science Data*, 16, 1965–2006,  
646 <https://doi.org/10.5194/essd-16-1965-2024>, 2024.

647 Chapman, D. C., Barth, J. A., Beardsley, R. C., and Fairbanks, R. G.: On the Continuity of Mean Flow between the  
648 Scotian Shelf and the Middle Atlantic Bight, *Journal of Physical Oceanography*, 16, 758–772,  
649 [https://doi.org/10.1175/1520-0485\(1986\)016<0758:OTCOMF>2.0.CO;2](https://doi.org/10.1175/1520-0485(1986)016<0758:OTCOMF>2.0.CO;2), 1986.

650 Cohen, J., Zhang, X., Francis, J., Jung, T., Kwok, R., Overland, J., Ballinger, T. J., Bhatt, U. S., Chen, H. W.,  
651 Coumou, D., Feldstein, S., Gu, H., Handorf, D., Henderson, G., Ionita, M., Kretschmer, M., Laliberte, F., Lee, S.,  
652 Linderholm, H. W., Maslowski, W., Peings, Y., Pfeiffer, K., Rigor, I., Semmler, T., Stroeve, J., Taylor, P. C.,  
653 Vavrus, S., Vihma, T., Wang, S., Wendisch, M., Wu, Y., and Yoon, J.: Divergent consensus on Arctic  
654 amplification influence on midlatitude severe winter weather, *Nat. Clim. Chang.*, 10, 20–29,  
655 <https://doi.org/10.1038/s41558-019-0662-y>, 2020.

656 Contreras Montoya, L. T., Lain, S., and Ilinca, A.: A Review on the Estimation of Power Loss Due to Icing in Wind  
657 Turbines, *Energies*, 15, 1083, <https://doi.org/10.3390/en15031083>, 2022.

658 Dehghani-Sanij, A. R., Dehghani, S. R., Naterer, G. F., and Muzychka, Y. S.: Sea spray icing phenomena on marine  
659 vessels and offshore structures: Review and formulation, *Ocean Engineering*, 132, 25–39,  
660 <https://doi.org/10.1016/j.oceaneng.2017.01.016>, 2017.

661 Donlon, C. J., Martin, M., Stark, J., Roberts-Jones, J., Fiedler, E., and Wimmer, W.: The Operational Sea Surface  
662 Temperature and Sea Ice Analysis (OSTIA) system, *Remote Sensing of Environment*, 116, 140–158,  
663 <https://doi.org/10.1016/j.rse.2010.10.017>, 2012.

664 Ferrel, W.: *Nashville Journal of Medicine and Surgery*, 11, 7–19,  
665 <https://empslocal.ex.ac.uk/people/staff/gv219/classics.d/ferrel-nashville56.pdf>, 1856.

666 Ferrier, B. S., Jin, Y., Lin, Y., Black, T., Rogers, E., and DiMego, G.: Implementation of a new grid-scale cloud and  
667 precipitation scheme in the NCEP Eta model, *Amer. Meteor. Soc. Conf. on Weather Analysis and Forecasting*, 19,  
668 [https://scholar.google.com/scholar?hl=en&as\\_sdt=0%2C6&q=Implementation+of+a+new+grid-](https://scholar.google.com/scholar?hl=en&as_sdt=0%2C6&q=Implementation+of+a+new+grid-scale+cloud+and+precipitation+scheme+in+the+NCEP+Eta+model&btnG=)  
669 [scale+cloud+and+precipitation+scheme+in+the+NCEP+Eta+model&btnG=](https://scholar.google.com/scholar?hl=en&as_sdt=0%2C6&q=Implementation+of+a+new+grid-scale+cloud+and+precipitation+scheme+in+the+NCEP+Eta+model&btnG=), 2002.

670 Fitch, A. C., Olson, J. B., Lundquist, J. K., Dudhia, J., Gupta, A. K., Michalakes, J., and Barstad, I.: Local and  
671 Mesoscale Impacts of Wind Farms as Parameterized in a Mesoscale NWP Model, *Monthly Weather Review*, 140,  
672 3017–3038, <https://doi.org/10.1175/MWR-D-11-00352.1>, 2012.

673 Fitch, A. C., Lundquist, J. K., and Olson, J. B.: Mesoscale Influences of Wind Farms throughout a Diurnal Cycle,  
674 *Mon. Wea. Rev.*, 141, 2173–2198, <https://doi.org/10.1175/MWR-D-12-00185.1>, 2013.

675 Gao, L. and Hong, J.: Wind turbine performance in natural icing environments: A field characterization, *Cold*  
676 *Regions Science and Technology*, 181, 103193, <https://doi.org/10.1016/j.coldregions.2020.103193>, 2021.

677 Gao, L. and Hu, H.: Wind turbine icing characteristics and icing-induced power losses to utility-scale wind turbines,  
678 *Proceedings of the National Academy of Sciences*, 118, e2111461118, <https://doi.org/10.1073/pnas.2111461118>,  
679 2021.

680 Geerts, B., Giangrande, S. E., McFarquhar, G. M., Xue, L., Abel, S. J., Comstock, J. M., Crewell, S., DeMott, P. J.,  
681 Ebell, K., Field, P., Hill, T. C. J., Hunzinger, A., Jensen, M. P., Johnson, K. L., Juliano, T. W., Kollias, P., Kosovic,  
682 B., Lackner, C., Luke, E., Lüpkes, C., Matthews, A. A., Neggers, R., Ovchinnikov, M., Powers, H., Shupe, M. D.,  
683 Spengler, T., Swanson, B. E., Tjernström, M., Theisen, A. K., Wales, N. A., Wang, Y., Wendisch, M., and Wu, P.:  
684 The COMBLE Campaign: A Study of Marine Boundary Layer Clouds in Arctic Cold-Air Outbreaks, *Bulletin of the*  
685 *American Meteorological Society*, 103, E1371–E1389, <https://doi.org/10.1175/BAMS-D-21-0044.1>, 2022.

686 Golbazi, M., Archer, C. L., and Alessandrini, S.: Surface impacts of large offshore wind farms, *Environ. Res. Lett.*,  
687 17, 064021, <https://doi.org/10.1088/1748-9326/ac6e49>, 2022.

688 Gómez, B. and Miguez-Macho, G.: The impact of wave number selection and spin-up time in spectral nudging,  
689 *Quarterly Journal of the Royal Meteorological Society*, 143, 1772–1786, <https://doi.org/10.1002/qj.3032>, 2017.

690 Gryning, S.-E., Batchvarova, E., Brümmner, B., Jørgensen, H., and Larsen, S.: On the extension of the wind profile  
691 over homogeneous terrain beyond the surface boundary layer, *Boundary-Layer Meteorol.*, 124, 251–268,  
692 <https://doi.org/10.1007/s10546-007-9166-9>, 2007.

693 Guest, P. and Luke, R.: The Power of Wind and Water, *Mariners Weather Log*,  
694 [https://www.vos.noaa.gov/MWL/dec\\_05/ves.shtml](https://www.vos.noaa.gov/MWL/dec_05/ves.shtml), 2005.

695 Hall, T. and Booth, J. F.: SynthETC: A Statistical Model for Severe Winter Storm Hazard on Eastern North  
696 America, *Journal of Climate*, 30, 5329–5343, <https://doi.org/10.1175/JCLI-D-16-0711.1>, 2017.

697 Hersbach, H., Bell, B., Berrisford, P., Hirahara, S., Horányi, A., Muñoz-Sabater, J., Nicolas, J., Peubey, C., Radu,  
698 R., Schepers, D., Simmons, A., Soci, C., Abdalla, S., Abellan, X., Balsamo, G., Bechtold, P., Biavati, G., Bidlot, J.,  
699 Bonavita, M., De Chiara, G., Dahlgren, P., Dee, D., Diamantakis, M., Dragani, R., Flemming, J., Forbes, R.,  
700 Fuentes, M., Geer, A., Haimberger, L., Healy, S., Hogan, R. J., Hólm, E., Janisková, M., Keeley, S., Laloyaux, P.,  
701 Lopez, P., Lupu, C., Radnoti, G., de Rosnay, P., Rozum, I., Vamborg, F., Villaume, S., and Thépaut, J.-N.: The  
702 ERA5 global reanalysis, *Quarterly Journal of the Royal Meteorological Society*, 146, 1999–2049,  
703 <https://doi.org/10.1002/qj.3803>, 2020.

704 Hirsch, R. M., Slack, J. R., and Smith, R. A.: Techniques of trend analysis for monthly water quality data, *Water*  
705 *Resources Research*, <https://doi.org/10.1029/WR018i001p00107>, 1982.

706 Hussain, M. M. and Mahmud, I.: pyMannKendall: a python package for non parametric Mann Kendall family of  
707 trend tests., *Journal of Open Source Software*, 4, 1556, <https://doi.org/10.21105/joss.01556>, 2019.

708 Iacono, M. J., Delamere, J. S., Mlawer, E. J., Shephard, M. W., Clough, S. A., and Collins, W. D.: Radiative forcing  
709 by long-lived greenhouse gases: Calculations with the AER radiative transfer models, *Journal of Geophysical*  
710 *Research: Atmospheres*, 113, <https://doi.org/10.1029/2008JD009944>, 2008.

711 IEA: Available Technologies for Wind Energy in Cold Climates – report, [https://iea-wind.org/wp-](https://iea-wind.org/wp-content/uploads/2021/09/Lehtomaki-et-al.-2018-Available-Technologies-for-Wind-Energy-in-Cold-Climates-report-2-nd-edition-2018.pdf)  
712 [content/uploads/2021/09/Lehtomaki-et-al.-2018-Available-Technologies-for-Wind-Energy-in-Cold-Climates-report-](https://iea-wind.org/wp-content/uploads/2021/09/Lehtomaki-et-al.-2018-Available-Technologies-for-Wind-Energy-in-Cold-Climates-report-2-nd-edition-2018.pdf)  
713 [2-nd-edition-2018.pdf](https://iea-wind.org/wp-content/uploads/2021/09/Lehtomaki-et-al.-2018-Available-Technologies-for-Wind-Energy-in-Cold-Climates-report-2-nd-edition-2018.pdf), 2018.

714 ISO: Atmospheric Icing of Structures, Geneva, Switzerland, ISO-12494:2017,  
715 <https://cdn.standards.iteh.ai/samples/72443/2fb2033c3f844304b66281607516ec58/ISO-12494-2017.pdf>, 2017.

716 Kain, J. S.: The Kain–Fritsch Convective Parameterization: An Update, *Journal of Applied Meteorology and*  
717 *Climatology*, 43, 170–181, [https://doi.org/10.1175/1520-0450\(2004\)043<0170:TKCPAU>2.0.CO;2](https://doi.org/10.1175/1520-0450(2004)043<0170:TKCPAU>2.0.CO;2), 2004.

718 Kraegel, L.: Destination likely sank after accumulating ice in heavy freezing spray, report says:  
719 [https://www.ktoo.org/2018/07/16/destination-likely-sank-after-accumulating-ice-in-heavy-freezing-spray-report-](https://www.ktoo.org/2018/07/16/destination-likely-sank-after-accumulating-ice-in-heavy-freezing-spray-report-says/)  
720 [says/](https://www.ktoo.org/2018/07/16/destination-likely-sank-after-accumulating-ice-in-heavy-freezing-spray-report-says/), last access: 12 April 2023.

721 Kraj, A. G. and Bibeau, E. L.: Phases of icing on wind turbine blades characterized by ice accumulation, *Renewable*  
722 *Energy*, 35, 966–972, <https://doi.org/10.1016/j.renene.2009.09.013>, 2010.

723 Line, W. E., Grasso, L., Hillger, D., Dierking, C., Jacobs, A., and Shea, S.: Using NOAA Satellite Imagery to Detect  
724 and Track Hazardous Sea Spray in the High Latitudes, *Weather and Forecasting*, 37, 351–369,  
725 <https://doi.org/10.1175/WAF-D-21-0137.1>, 2022.

726 NTSB: NTSB announces the probable cause of the sunken Scandies Rose:  
727 <https://www.alaskasnews.com/2021/06/29/ntsb-announce-probable-cause-sunken-scandies-rose/>, last access:  
728 12 April 2023.

729 Madi, E., Pope, K., Huang, W., and Iqbal, T.: A review of integrating ice detection and mitigation for wind turbine  
730 blades, *Renewable and Sustainable Energy Reviews*, 103, 269–281, <https://doi.org/10.1016/j.rser.2018.12.019>,  
731 2019.

732 Martini, F., Contreras Montoya, L. T., and Ilinca, A.: Review of Wind Turbine Icing Modelling Approaches,  
733 *Energies*, 14, 5207, <https://doi.org/10.3390/en14165207>, 2021.

734 Monahan, E. C. and MacNiocaill, G.: *Oceanic Whitecaps And Their Role in Air-Sea Exchange Processes*, D Reidel  
735 Publishing Company, e-ISBN-13: 978-94-009-4668-2, <https://link.springer.com/book/10.1007/978-94-009-4668-2>,  
736 1986.

737 Monahan, E. C., Fairall, C. W., Davidson, K. L., and Boyle, P. J.: Observed inter-relations between 10m winds,  
738 ocean whitecaps and marine aerosols, *Quarterly Journal of the Royal Meteorological Society*, 109, 379–392,  
739 <https://doi.org/10.1002/qj.49710946010>, 1983.

740 Monin, A. S. and Obukhov, A. M.: Basic laws of turbulent mixing in the surface layer of the atmosphere, *Tr. Akad.*  
741 *Nauk SSSR Geophys. Inst.*, 24, 30, [https://gibbs.science/efd/handouts/monin\\_obukhov\\_1954.pdf](https://gibbs.science/efd/handouts/monin_obukhov_1954.pdf), 1954.

742 Musial, W., Spitsen, P., Duffy, P., Beiter, P., Marquis, M., Hammond, R., and Shields, M.: *Offshore Wind Market*  
743 *Report: 2022 Edition*, NREL/TP-5000-83544, National Renewable Energy Laboratory, Golden, CO (United States),  
744 <https://doi.org/10.2172/188338>, 2022.

745 Nakanishi, M. and Niino, H.: An Improved Mellor–Yamada Level-3 Model: Its Numerical Stability and Application  
746 to a Regional Prediction of Advection Fog, *Boundary-Layer Meteorol.*, 119, 397–407,  
747 <https://doi.org/10.1007/s10546-005-9030-8>, 2006.



748 Nilsen, T.: Icing believed to cause sinking of fishing boat in Barents Sea, 17 missing:  
749 [https://thebarentsobserver.com/en/2020/12/icing-believed-cause-sining-fishing-boat-barents-sea-17-missing](https://thebarentsobserver.com/en/2020/12/icing-believed-cause-sinking-fishing-boat-barents-sea-17-missing), last  
750 access: 12 April 2023.

751 Niu, G.-Y., Yang, Z.-L., Mitchell, K. E., Chen, F., Ek, M. B., Barlage, M., Kumar, A., Manning, K., Niyogi, D.,  
752 Rosero, E., Tewari, M., and Xia, Y.: The community Noah land surface model with multiparameterization options  
753 (Noah-MP): 1. Model description and evaluation with local-scale measurements, *Journal of Geophysical Research:*  
754 *Atmospheres*, 116, <https://doi.org/10.1029/2010JD015139>, 2011.

755 Novacheck, J., Sharp, J., Schwarz, M., Donohoo-Vallett, P., Tzavelis, Z., Buster, G., and Rossol, M.: The Evolving  
756 Role of Extreme Weather Events in the U.S. Power System with High Levels of Variable Renewable Energy,  
757 NREL/TP-6A20-78394, 1837959, MainId:32311, NREL/TP-6A20-78394, 1837959, MainId:32311,  
758 <https://doi.org/10.2172/1837959>, 2021.

759 NREL: 2023 National Offshore Wind data set (NOW-23), <https://dx.doi.org/10.25984/1821404>, 2020.

760 Glossary - NOAA's National Weather Service: <https://w1.weather.gov/glossary/index.php?word=freezing+spray>,  
761 last access: 12 April 2023.

762 Nygaard, N. G.: Wakes in very large wind farms and the effect of neighbouring wind farms, *J. Phys.: Conf. Ser.*,  
763 524, 012162, <https://doi.org/10.1088/1742-6596/524/1/012162>, 2014.

764 Overland, J. E.: Prediction of Vessel Icing for Near-Freezing Sea Temperatures, *Weather and Forecasting*, 5, 62–77,  
765 [https://doi.org/10.1175/1520-0434\(1990\)005<0062:POVIFN>2.0.CO;2](https://doi.org/10.1175/1520-0434(1990)005<0062:POVIFN>2.0.CO;2), 1990.

766 Overland, J. E., Pease, C. H., Preisendorfer, R. W., and Comiskey, A. L.: Prediction of Vessel Icing, *Journal of*  
767 *Applied Meteorology and Climatology*, 25, 1793–1806, [https://doi.org/10.1175/1520-0450\(1986\)025<1793:POVI>2.0.CO;2](https://doi.org/10.1175/1520-0450(1986)025<1793:POVI>2.0.CO;2), 1986.

769 Parent, O. and Ilinca, A.: Anti-icing and de-icing techniques for wind turbines: Critical review, *Cold Regions*  
770 *Science and Technology*, 65, 88–96, <https://doi.org/10.1016/j.coldregions.2010.01.005>, 2011.

771 Platis, A., Siedersleben, S. K., Bange, J., Lampert, A., Bärfuss, K., Hankers, R., Cañadillas, B., Foreman, R.,  
772 Schulz-Stellenfleth, J., Djath, B., Neumann, T., and Emeis, S.: First in situ evidence of wakes in the far field behind  
773 offshore wind farms, *Sci Rep*, 8, 2163, <https://doi.org/10.1038/s41598-018-20389-y>, 2018.

774 Powers, J. G., Klemp, J. B., Skamarock, W. C., Davis, C. A., Dudhia, J., Gill, D. O., Coen, J. L., Gochis, D. J.,  
775 Ahmadov, R., Peckham, S. E., Grell, G. A., Michalakes, J., Trahan, S., Benjamin, S. G., Alexander, C. R., Dimego,  
776 G. J., Wang, W., Schwartz, C. S., Romine, G. S., Liu, Z., Snyder, C., Chen, F., Barlage, M. J., Yu, W., and Duda,  
777 M. G.: The Weather Research and Forecasting Model: Overview, System Efforts, and Future Directions, *Bulletin of*  
778 *the American Meteorological Society*, 98, 1717–1737, <https://doi.org/10.1175/BAMS-D-15-00308.1>, 2017.

779 Pronk, V., Bodini, N., Optis, M., Lundquist, J. K., Moriarty, P., Draxl, C., Purkayastha, A., and Young, E.: Can  
780 reanalysis products outperform mesoscale numerical weather prediction models in modeling the wind resource in  
781 simple terrain?, *Wind Energy. Sci.*, 7, 487–504, <https://doi.org/10.5194/wes-7-487-2022>, 2022.

782 Quint, D., Lundquist, J. K., Bodini, N., and Rosencrans, D.: Meteorological Impacts of Offshore Wind Turbines as  
783 Simulated in the Weather Research and Forecasting Model, *Wind Energy Science Discussions*, 1–34,  
784 <https://doi.org/10.5194/wes-2024-53>, 2024.

785 Rajewski, D. A., Takle, E. S., Lundquist, J. K., Oncley, S., Prueger, J. H., Horst, T. W., Rhodes, M. E., Pfeiffer, R.,  
786 Hatfield, J. L., Spoth, K. K., and Doorenbos, R. K.: Crop Wind Energy Experiment (CWEX): Observations of  
787 Surface-Layer, Boundary Layer, and Mesoscale Interactions with a Wind Farm, *Bulletin of the American*  
788 *Meteorological Society*, 94, 655–672, <https://doi.org/10.1175/BAMS-D-11-00240.1>, 2013.

789 Redfern, S., Optis, M., Xia, G., and Draxl, C.: Offshore wind energy forecasting sensitivity to sea surface  
790 temperature input in the Mid-Atlantic, *Wind Energy Science*, 8, 1–23, <https://doi.org/10.5194/wes-8-1-2023>, 2023.

791 Rosencrans, D., Lundquist, J. K., Optis, M., Rybchuk, A., Bodini, N., and Rossol, M.: Seasonal variability of wake  
792 impacts on US mid-Atlantic offshore wind plant power production, *Wind Energy Science*, 9, 555–583,  
793 <https://doi.org/10.5194/wes-9-555-2024>, 2024.

794 Ross, D. B. and Cardone, V.: Observations of oceanic whitecaps and their relation to remote measurements of  
795 surface wind Speed, *Journal of Geophysical Research* (1896-1977), 79, 444–452,  
796 <https://doi.org/10.1029/JC079i003p00444>, 1974.

797 Russell, L. M.: Sea-spray particles cause freezing in clouds, *Nature*, 525, 194–195, <https://doi.org/10.1038/525194a>,  
798 2015.

799 Schneemann, J., Rott, A., Dörenkämper, M., Steinfeld, G., and Kühn, M.: Cluster wakes impact on a far-distant  
800 offshore wind farm's power, *Wind Energy Science*, 5, 29–49, <https://doi.org/10.5194/wes-5-29-2020>, 2020.

801 Shcherbina, A. Y. and Gawarkiewicz, G. G.: A coastal current in winter: 2. Wind forcing and cooling of a coastal  
802 current east of Cape Cod, *Journal of Geophysical Research: Oceans*, 113, <https://doi.org/10.1029/2008JC004750>,  
803 2008a.

804 Shcherbina, A. Y. and Gawarkiewicz, G. G.: A coastal current in winter: Autonomous underwater vehicle  
805 observations of the coastal current east of Cape Cod, *Journal of Geophysical Research: Oceans*, 113,  
806 <https://doi.org/10.1029/2007JC004306>, 2008b.

807 Siedersleben, S. K., Lundquist, J. K., Platis, A., Bange, J., Bärfuss, K., Lampert, A., Cañadillas, B., Neumann, T.,  
808 and Emeis, S.: Micrometeorological impacts of offshore wind farms as seen in observations and simulations,  
809 *Environ. Res. Lett.*, 13, 124012, <https://doi.org/10.1088/1748-9326/aaea0b>, 2018.

810 Stull, B. R.: An Introduction to Boundary Layer Meteorology, Springer Science & Business Media,  
811 [https://books.google.com/books?hl=en&lr=&id=2PjrCAAAQBAJ&oi=fnd&pg=PR10&dq=An+Introduction+to+Boundary+Layer+Meteorology+stull&ots=BdY\\_2W6EQ2&sig=eLi51Vaua4aeHUWQt-NfG0IkTM#v=onepage&q=An%20Introduction%20to%20Boundary%20Layer%20Meteorology%20stull&f=false](https://books.google.com/books?hl=en&lr=&id=2PjrCAAAQBAJ&oi=fnd&pg=PR10&dq=An+Introduction+to+Boundary+Layer+Meteorology+stull&ots=BdY_2W6EQ2&sig=eLi51Vaua4aeHUWQt-NfG0IkTM#v=onepage&q=An%20Introduction%20to%20Boundary%20Layer%20Meteorology%20stull&f=false),  
812 1988.

815 SWAN Team: Scientific and Technical Documentation (SWAN Cycle III version 41.31A), Delft University of  
816 Technology, <https://swanmodel.sourceforge.io/download/zip/swantech.pdf>, 2020.

817 Tewari, M., Chen, F., Wang, W., Dudhia, J., LeMone, M., Mitchell, K., Ek, M., Gayno, G., Wegiel, J., and Cuenca,  
818 R. H.: (PDF) Implementation and verification of the united NOAH land surface model in the WRF model,  
819 *Proceedings of the 20th conference on weather analysis and forecasting/16th conference on numerical weather*  
820 *prediction*, 14,  
821 [https://www.researchgate.net/publication/286272692\\_Implementation\\_and\\_verification\\_of\\_the\\_united\\_NOAH\\_land](https://www.researchgate.net/publication/286272692_Implementation_and_verification_of_the_united_NOAH_land_surface_model_in_the_WRF_model)  
822 [\\_surface\\_model\\_in\\_the\\_WRF\\_model](https://www.researchgate.net/publication/286272692_Implementation_and_verification_of_the_united_NOAH_land_surface_model_in_the_WRF_model), 2004.

823 Thompson, G., Field, P. R., Rasmussen, R. M., and Hall, W. D.: Explicit Forecasts of Winter Precipitation Using an  
824 Improved Bulk Microphysics Scheme. Part II: Implementation of a New Snow Parameterization, *Monthly Weather*  
825 *Review*, 136, 5095–5115, <https://doi.org/10.1175/2008MWR2387.1>, 2008.

826 Tolman, H., Abdolali, A., Accensi, M., Alves, J.-H., Arduin, F., Babanin, A., Barbariol, F., Benetazzo, A., Bidlot,  
827 J., Booij, N., Boutin, G., Bunney, C., Campbell, T., Chalikov, D., Chawla, A., Cheng, S., Collins III, C., Filipot, J.-  
828 F., Flampouris, S., and Liang, Z.: User manual and system documentation of WAVEWATCH III (R) version 6.07,  
829 [https://www.researchgate.net/publication/336069899\\_User\\_manual\\_and\\_system\\_documentation\\_of\\_WAVEWATCH](https://www.researchgate.net/publication/336069899_User_manual_and_system_documentation_of_WAVEWATCH_III_R_version_607)  
830 [\\_III\\_R\\_version\\_607](https://www.researchgate.net/publication/336069899_User_manual_and_system_documentation_of_WAVEWATCH_III_R_version_607), 2019.

831 Tomaszewski, J. M. and Lundquist, J. K.: Simulated wind farm wake sensitivity to configuration choices in the  
832 Weather Research and Forecasting model version 3.8.1, *Geoscientific Model Development*, 13, 2645–2662,  
833 <https://doi.org/10.5194/gmd-13-2645-2020>, 2020.

834 U.S. Navy: U. S. Navy Cold Weather Handbook for Surface Ships, Surface Ship Survivability Office,  
835 <https://media.defense.gov/2021/Feb/25/2002588484/-1/-1/0/CG%20070%20-%20US%20NAVY%20COLD%20WEATHER%20HANDBOOK.PDF>, 1988.

837 Vavrus, S., Walsh, J. E., Chapman, W. L., and Portis, D.: The behavior of extreme cold air outbreaks under  
838 greenhouse warming, *International Journal of Climatology*, 26, 1133–1147, <https://doi.org/10.1002/joc.1301>, 2006.

839 Wallace, J. M. and Hobbs, P. V.: *Atmospheric Science: An Introductory Survey*, 2nd ed., Elsevier, University of  
840 Washington, ISBN:978-0-12-732951-2, 2006.

841 Wei, K., Yang, Y., Zuo, H., and Zhong, D.: A review on ice detection technology and ice elimination technology for  
842 wind turbine, *Wind Energy*, 23, 433–457, <https://doi.org/10.1002/we.2427>, 2020.

843 Winters, A. C., Bosart, L. F., and Keyser, D.: Antecedent North Pacific Jet Regimes Conducive to the Development  
844 of Continental U.S. Extreme Temperature Events during the Cool Season, *Weather and Forecasting*, 34, 393–414,  
845 <https://doi.org/10.1175/WAF-D-18-0168.1>, 2019.

846 Xia, G., Zhou, L., Freedman, J. M., Roy, S. B., Harris, R. A., and Cervarich, M. C.: A case study of effects of  
847 atmospheric boundary layer turbulence, wind speed, and stability on wind farm induced temperature changes using  
848 observations from a field campaign, *Clim Dyn*, 46, 2179–2196, <https://doi.org/10.1007/s00382-015-2696-9>, 2016.

849  
850